Computer Methods in Applied Mechanics and Engineering 441 (2025) 117980

Contents lists available at ScienceDirect

Comput. Methods Appl. Mech. Engrg.

journal homepage: www.elsevier.com/locate/cma

A novel data-driven digital reconstruction method for polycrystalline microstructures

Bingbing Chen [a], Dongfeng Li [b], Liyuan Wang [a], Xiangyun Ge [a], Chenfeng Li [a,*]

[a] Zienkiewicz Institute for Modelling, Data and AI, Faculty of Science and Engineering, Swansea University, SA1 8EN, United Kingdom
[b] School of Science, Harbin Institute of Technology, Shenzhen, 518055, China

ARTICLE INFO

Keywords:
Alloy material
Crystal plasticity finite element
Microstructural reconstruction
Representative volume element
Structure–property linkage
Electron backscatter diffraction

ABSTRACT

Data-driven digital reconstruction is a power tool for building digital microstructures for such heterogeneous materials as porous media and composites. It uses scanned images as reference and generates digital microstructures through optimisation procedures or computer vision methods. However, data-driven digital reconstruction methods do not apply to polycrystalline microstructures because their raw measurement data (lattice orientation, grain structure, and phase distribution) do not naturally correspond to RGB images. It faces challenges such as discontinuities and ambiguities in orientation colouring, as well as a lack of algorithms for extracting orientation data from RGB images. This paper introduces a novel data-driven digital reconstruction method for polycrystalline microstructures. The method includes experimental acquisition of microstructural data (such as phase map, lattice symmetry, and lattice orientation), conversion of experimental data to RGB image formats for continuous and symmetry-conserved visualisation, image generation from continuous and symmetry-conserved orientation colouring, and reconstruction of grain data from synthesised RGB images. The results demonstrate that this method enables efficient microstructure reconstructions with high fidelity to actual microstructural characteristics, addressing the limitations of traditional methods. Furthermore, by offering realistic digital microstructure models, this novel data-driven reconstruction scheme can be readily integrated with simulation tools to improve the study of structure–property linkages in polycrystalline materials.

1. Introduction

Polycrystalline materials, including metals [1,2], rocks [3], and ceramics [4], are prevalent in nature and industry. Their formation involves nucleation and growth via solidification, recrystallisation, grain growth, and solid-state phase transformation. These complex evolution processes lead to polycrystalline microstructures with random crystallographic and morphological features, comprising grain aggregates with varying lattice orientations, sizes, and shapes, separated by grain boundaries. Random characteristics of polycrystalline microstructures significantly influence macroscopic properties and performance of polycrystalline materials [1,4]. Advancements in microscopic imaging, especially Orientation Imaging Microscopy (OIM), have enabled high-fidelity quantitative microstructure characterisation of polycrystalline materials. Polycrystalline microstructure characteristics are commonly described using various statistical descriptors, such as phase volume fraction, grain size [5], grain orientation [5], grain boundary [6], and chord length [7].

* Corresponding author.
E-mail address: c.f.li@swansea.ac.uk (C. Li).

https://doi.org/10.1016/j.cma.2025.117980
Received 15 January 2025; Received in revised form 3 March 2025; Accepted 26 March 2025

Microstructure reconstruction of polycrystalline materials creates digital polycrystalline microstructures that match those found in real solids. These digital microstructures are commonly termed Representative Volume Elements (RVEs), representing the smallest material volume that is sufficiently large to assess the macroscopic material properties of the corresponding solid [8]. Microstructure reconstruction techniques for polycrystalline materials can be divided into experimental and non-experimental approaches [9].

Experimental reconstruction methods employ imaging technologies such as Scanning Electron Microscopy (SEM) [10], Electron Backscattering Diffraction (EBSD) [11], X-ray microtomography [12], and X-ray diffraction [13] to provide high-resolution, direct observations of lattice orientation, grain structure, and phase distribution. Experimental reconstruction offers first-hand physically accurate data crucial for understanding the complex, random characteristics influencing macroscopic properties and performance.

Non-experimental reconstruction methods can be generally divided into two categories: physics-based and geometry-based approaches [9,14]. Typical physics-based approaches include cellular automata [15,16], Monte Carlo simulations [17–19], vertex/front tracking [20,21], level set methods [22–24], and phase-field techniques [25]. They replicate microstructure formation processes, including nucleation, solidification, recrystallisation, grain growth, and solid-state phase transformations. These methods offer flexibility in capturing the influence of various processing parameters, such as temperature, diffusion coefficients, and strain rates, on microstructural evolution. In contrast, geometry-based approaches, such as Voronoi tessellation [14,26], ellipsoid packing [27–35], high-order methods [36–39] and reduced-order methods [40–43], operate directly on the morphological and crystallographic information of polycrystalline materials while ignoring the evolutionary processes of microstructural formation. These methods have advantages in computational efficiency and scalability, enabling rapid and large-scale polycrystalline microstructure reconstruction.

Despite their strengths, both experimental and non-experimental reconstruction approaches have significant limitations. Experimental methods are often resource-intensive and face limitation in equipment capacity and sample availability. Furthermore, fully capturing the inherent randomness of polycrystalline microstructures remains challenging, particularly when attempting to effectively sample the vast parameter space. For physics-based methods, underlying assumptions, such as those related to thermal nucleation, solute diffusion, and grain growth, are often idealised, limiting their ability to reproduce realistic microstructures. While computationally efficient, geometry-based methods generally fail to account for the complex and heterogeneous nature of real-world grains, often simplifying grain geometry to regular shapes, such as ellipsoids or Voronoi cells, thus overlooking the intricate, irregular geometries observed in actual materials.

This paper introduces a novel data-driven method for digitally reconstructing polycrystalline microstructures to address these challenges. The approach involves transforming raw measurement data of polycrystalline microstructures into reference images, generating new images using texture synthesis techniques, and subsequently converting the newly generated images back into polycrystalline microstructure data. This method integrates the advantages of both experimental and non-experimental approaches, offering a comprehensive solution that combines the accuracy of experimental data with the efficiency of computational methods. As illustrated in Fig. 1, the proposed data-driven approach consists of four key steps: (1) the experimental acquisition of microstructural data, such as lattice symmetry and orientation, from various imaging techniques; (2) the conversion of these experimental data into RGB images; (3) image generation using the image coloured in step 2 as reference; and (4) the reconstruction of grain data from the synthesised RGB images obtained in step 3.

The key technical challenge for this data-driven digital reconstruction approach lies in the information transformation between polycrystalline microstructures and RGB images. Orientation colour maps commonly used for visualising polycrystalline microstructures often directly map Euler angles $(\varphi_1, \phi, \varphi_2)$ or Rodrigues-Frank vectors (ρ_1, ρ_2, ρ_3) to RGB components [44–46]. This leads to topological mismatches between the disconnected orientation space and the connected RGB colour space, resulting in colour discontinuities and visual artefacts [47,48]. Moreover, neglecting crystal symmetry induces colour ambiguity, where identical crystallographic orientations are represented by different colours, further complicating the interpretation of the microstructure. Additionally, no algorithms exist to extract orientation data from RGB images, limiting their applicability for comprehensive microstructure reconstructions [49].

In this research, we address orientation colouring challenges by adapting the Inverse Pole Figure (IPF) colouring technique to resolve issues of colour discontinuities and ambiguity and developing an inverse orientation colouring algorithm to extract orientation data from synthesised RGB images. For image generation, a patch-based texture synthesis algorithm, combined with image quilting techniques and fast template matching schemes. Finally, as a demonstration use case, the crystal plasticity finite element simulation is integrated with the proposed data-driven digital reconstructions to establish structure–property linkages. The remainder of the paper is organised into five sections. Section 2 introduces the proposed orientation colour mapping strategies, Section 3 presents image generation from continuous and symmetry-conserved orientation colouring, and Section 4 examines the performance of the proposed data-driven digital reconstruction method and demonstrates its application using a real polycrystalline material. Finally, Section 5 summarises conclusions and future work.

2. Orientation colour mapping strategies

2.1. Orientation to colour mapping

In polycrystalline materials, lattice orientation $\boldsymbol{G}$ defines the rotational relationship between the reference frame and single crystal axes. As summarised in Table 1, the lattice orientation can be captured by different parameterisation schemes, and they each require three independent parameters [47]. Lattice orientation colouring is essential for microstructural visualisation of polycrystalline materials, where different grains are marked with different colours clearly illustrating the morphological features of polycrystalline microstructures.

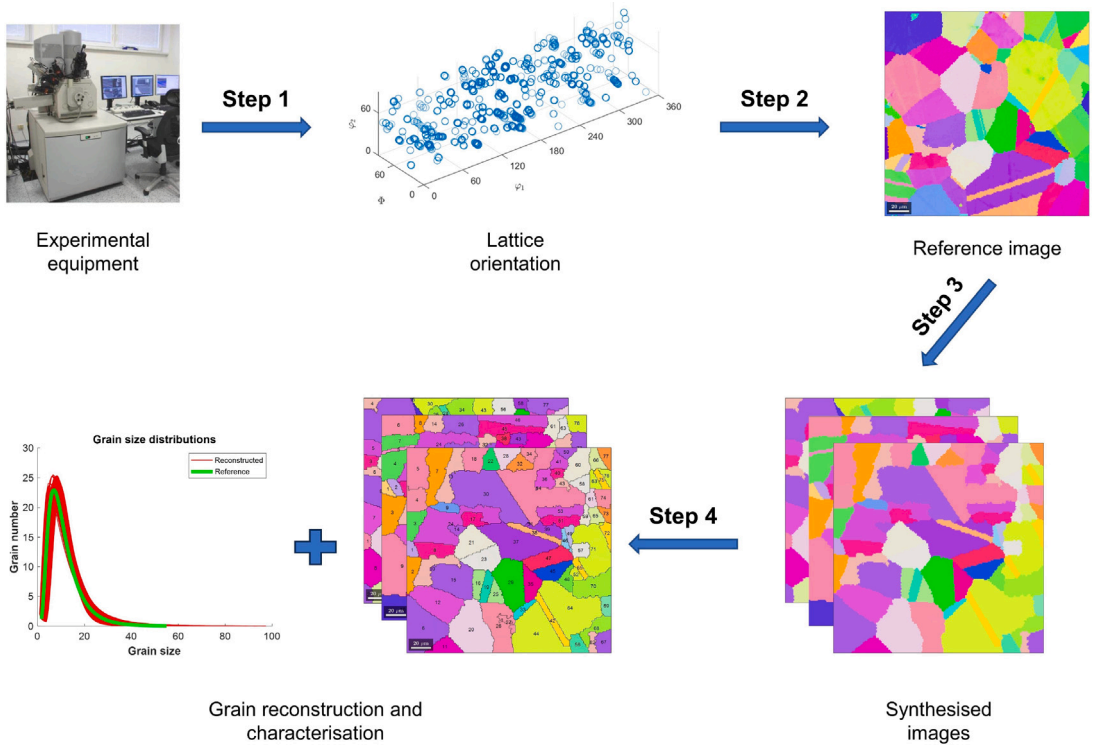

Fig. 1. Flowchart of the novel data-driven digital reconstruction method. (For interpretation of the references to colour in this figure legend, the reader is referred to the web version of this article.)

Table 1
Summary of lattice orientation parameterisations.

Name	Parameters	Definition
Euler angles	$(\varphi_1, \phi, \varphi_2)$	$\boldsymbol{G} = (g_{ij}) = \begin{pmatrix} cos\varphi_1 cos\varphi_2 - sin\varphi_1 sin\varphi_2 cos\phi & sin\varphi_1 cos\varphi_2 + cos\varphi_1 sin\varphi_2 cos\phi & sin\varphi_2 sin\phi \\ -cos\varphi_1 sin\varphi_2 - sin\varphi_1 cos\varphi_2 cos\phi & -sin\varphi_1 sin\varphi_2 + cos\varphi_1 cos\varphi_2 cos\phi & cos\varphi_2 sin\phi \\ sin\varphi_1 sin\phi & -cos\varphi_1 sin\phi & cos\phi \end{pmatrix}$
Miller indices	$(hkl)[uvw]$	$\boldsymbol{G} = (g_{ij}) = \begin{pmatrix} \frac{u}{\sqrt{u^2+v^2+w^2}} & \frac{r}{\sqrt{r^2+s^2+t^2}} & \frac{h}{\sqrt{h^2+k^2+l^2}} \\ \frac{v}{\sqrt{u^2+v^2+w^2}} & \frac{s}{\sqrt{r^2+s^2+t^2}} & \frac{k}{\sqrt{h^2+k^2+l^2}} \\ \frac{w}{\sqrt{u^2+v^2+w^2}} & \frac{t}{\sqrt{r^2+s^2+t^2}} & \frac{l}{\sqrt{h^2+k^2+l^2}} \end{pmatrix}$
Matrix	a_{ij}	$\boldsymbol{G} = (g_{ij}) = \begin{pmatrix} a_{11} & a_{12} & a_{13} \\ a_{21} & a_{22} & a_{23} \\ a_{31} & a_{32} & a_{33} \end{pmatrix}$
Axis-angle	$(\theta, \boldsymbol{n})$	$g_{ij} = \delta_{ij} cos\theta + n_i n_j (1 - cos\theta) + \sum_{k=1,3} \xi_{ijk} n_k sin\theta$
Rodrigues-Frank vector	(ρ_1, ρ_2, ρ_3)	$(\rho_1, \rho_2, \rho_3) = tan(\theta/2)\boldsymbol{n}$
Quaternion	$q = (q_1, q_2, q_3, q_4)$	$(\boldsymbol{q}, q_4) = (sin(\theta/2)\boldsymbol{n}, cos(\theta/2))$

Direct colourmaps between the orientation and colour spaces are commonly used for orientation colouring [44–46]. However, improvements are needed, particularly regarding topological inconsistencies between orientation and colour spaces. Colour spaces, such as Hue-Saturation-Value (HSV), Hue-Saturation-Lightness (HSL) and Red–Green–Blue (RGB), are simply connected spaces in three-dimensional Euclidean ($\boldsymbol{R^3}$) space, and any closed path within the colour spaces can deform or shrink to a single point. In contrast, orientation spaces are not inherently linked and cannot be incorporated into the $\boldsymbol{R^3}$ space [47]. Although three independent orientational parameters define components in an RGB triplet, $\boldsymbol{G}$ cannot be continuously mapped one-to-one to any space lower than five dimensions [50]. Additionally, ignoring crystal symmetry can lead to colour ambiguity, where symmetrically equivalent orientations may be represented by different colours [48].

To resolve visualisation challenges in direct orientation-to-colour mapping, IPF colouring has been systematically extended to enhance orientation colouring [48], and its workflow is summarised in Fig. 2. The first step (see Fig. 2.a) is to define a vector $\boldsymbol{r}$ representing the Normal Direction (ND) in the specimen coordinate system, and then transform it into the vector $\boldsymbol{h}$ in the crystal coordinate system as:

$$\boldsymbol{h} = \boldsymbol{G}^{-1} \boldsymbol{r}_{ND} \tag{1}$$

Table 2
Symmetry groups are characterised by lattice types, standard or extended colour distributions, with k defining the relative order of groups. Standard and extended colour distributions are unsuitable for $\bar{3}, \bar{4}$, and $\bar{1}$, which are listed in the "Exception" column.

Lattice type	Standard		Extended					Exception
	k	$\boldsymbol{P}_+$	k	$\boldsymbol{P}$				
Cubic	48	$m\bar{3}m$	24	432	$m\bar{3}$			
	24	$\bar{4}3m$	12	23				
Hexagonal, trigonal	24	$6/mmm$	12	622	$6/m$	$\bar{3}m1$	$\bar{3}1m$	$\bar{3}$
	12	$\bar{6}2m$, $\bar{6}m2$	6	$\bar{6}$	321	312		
	12	$6mm$	6	6				
	6	$3m1$	6	3				
Tetragonal	16	$4/mmm$	8	422	$\bar{4}2m$	$\bar{4}m2$	$4/m$	$\bar{4}$
	8	$4mm$	4	4				
Orthorhombic, monoclinic	8	mmm	4	222	$112/m$	$12/m1$		
	4	$mm2$	2	112				
	4	$m2m$, $2mm$	2	121				
Triclinic	2	$1m1$	1	1				$\bar{1}$

where $\boldsymbol{G}$ is the lattice orientation (see Table 1). As shown in Fig. 2.b, all crystallographically distinct vectors $\boldsymbol{h}$ define a fundamental sector of symmetry group $\boldsymbol{P}$, and each point h in fundamental sector corresponds to a unique vector $\boldsymbol{h}$. As shown in Fig. 2.c, the location of h in the fundamental sector is defined by two variables: the polar angle θ and the azimuthal angle ρ. Ranging from 0° to 90° on the HSL colourisation of upper unit hemisphere and from 90° to 180° on the HSL colourisation of lower unit hemisphere, the polar angle θ is determined by the line distance d_{hp} between the point h and the barycentre p of fundamental sector. The line distance d_{hp} corresponds proportionally to the polar angle θ such that the maximum distance corresponds to 90° in the upper unit hemisphere or 180° in the lower unit hemisphere. The angle between the line pA and the line ph defines angle ρ, ranging from 0° to 360°. Asymmetric HSL distributions are calculated using θ and ρ to achieve the one-to-one colouring of h. The key steps for the extended IPF orientation colouring are outlined below for completeness, while algorithm details can be found in [48].

- Customised hue gradient: Hue H, representing azimuthal angle ρ, is expressed as:

$$H = \int_0^{\omega} v(\rho) d\rho \tag{2}$$

where $v(\rho)$ is the speed function defined as:

$$v(\rho) = d(\rho)\left(0.5 + e^{-\frac{4}{7}[\rho]^2} + e^{-\frac{4}{7}\left[\rho - \frac{2\pi}{3}\right]^2} + e^{-\frac{4}{7}\left[\rho + \frac{2\pi}{3}\right]^2}\right) \tag{3}$$

where $d(\rho)$ denotes the distance between the barycentre p and the boundary point b in the fundamental sector. Interior angles ω_1, ω_2, ω_3 (see Fig. 2.c) within the fundamental sector may vary significantly. To address these angle differences, the speed function is normalised as:

$$\int_0^{\omega_1} v(\rho) d\rho = \int_{\omega_1}^{\omega_1+\omega_2} v(\rho) d\rho = \int_{\omega_1+\omega_2}^{2\pi} v(\rho) d\rho = \frac{1}{3} \tag{4}$$

- Nonlinear lightness scaling: A nonlinear scaling map between lightness L and θ is introduced to achieve a more balanced representation, defined as:

$$L = \lambda_L \frac{\theta}{\pi} + (1 - \lambda_L) sin^2 \frac{\theta}{2} \tag{5}$$

where the parameter λ_L adjusts the central white or black region size in IPF colouring.

- Lightness dependent saturation: Lightness-dependent saturation S has been proposed to colour the central region with bright or dark grey, expressed as:

$$S = 1 - 2\lambda_S |L - 0.5| \tag{6}$$

where the parameter λ_S specifies the degree of grey in the centre.

There are several inherent advantages in the above IPF colouring that respects the symmetry group $\boldsymbol{P}$. First, the fundamental sector of symmetry group $\boldsymbol{P}$ ensures that similar orientations correspond to similar colours. Second, asymmetric HSL distribution can correlate colour differences with misorientation angle size. Most importantly, discontinuity-free colour distributions are achievable when each boundary in fundamental sector is a crystallographic mirror plane. Specifically, let R denote the central rotation axis, symmetry groups satisfying conditions (a) $2 \perp R$ and (b) $2 \perp \bar{2}$ enable smooth colour transitions at fundamental sector boundaries using standard asymmetric HSL distribution. Table 2 summarises symmetry groups satisfying this condition in the "Standard" column. Examples include $m\bar{3}m$, $\bar{4}3m$, $6/mmm$, $\bar{6}2m$, $\bar{6}m2$, $6mm$, $3m1$, $4/mmm$, $4mm$, mmm, $mm2$, $m2m$, $2mm$, and $1m1$.

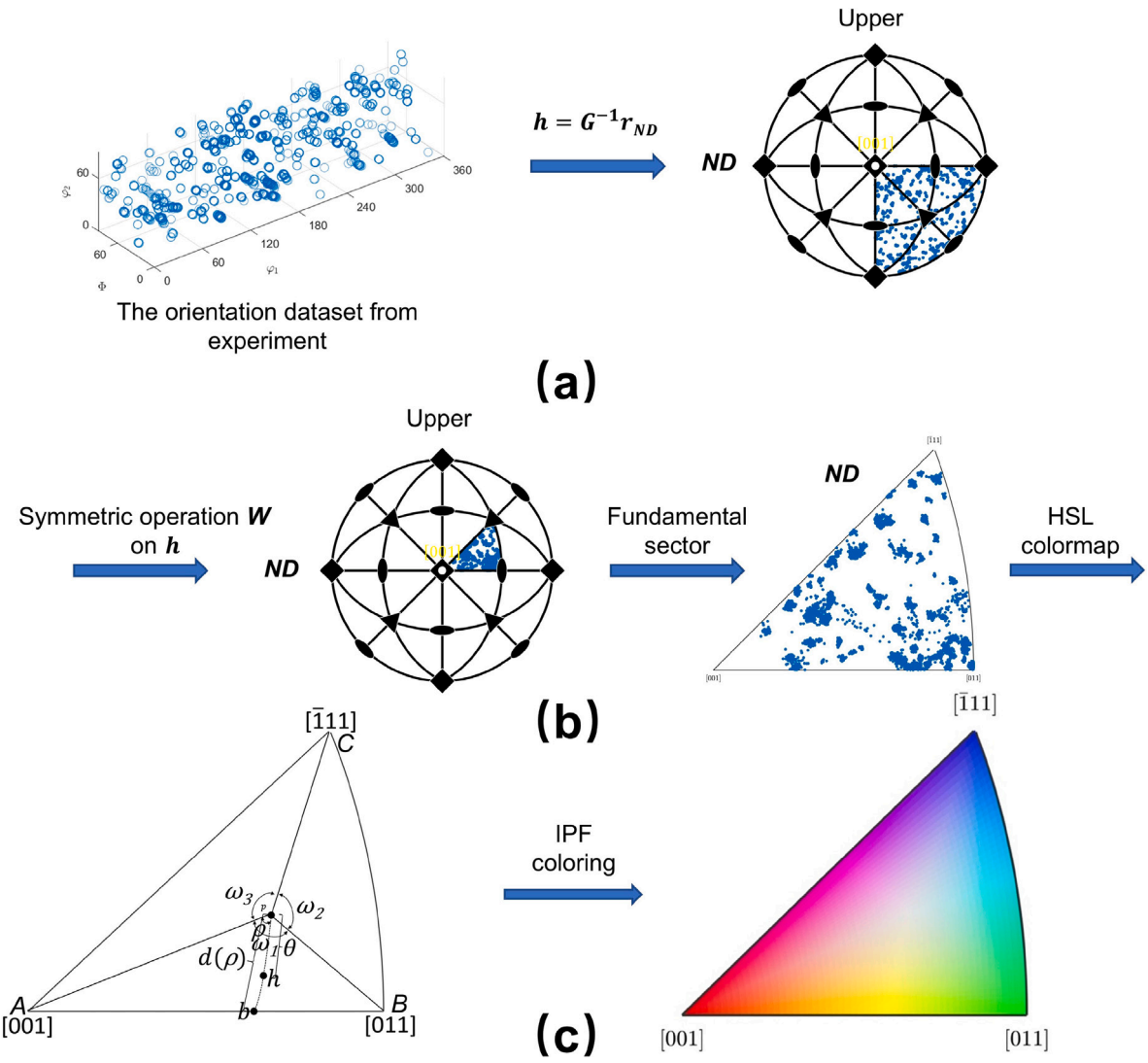

Fig. 2. Flowchart of IPF colouring for $m\bar{3}m$ symmetry group. (For interpretation of the references to colour in this figure legend, the reader is referred to the web version of this article.)

Symmetry groups are categorised by order k and lattice types in Table 2. The order k of symmetry groups determines fundamental sector's equivalent size but not shape. For any symmetry group $\boldsymbol{P}$ listed under the "Extended" column, its order is half that of the corresponding supersymmetry group $\boldsymbol{P}_+$ in the "standard" column. Thus, the diversity of $\boldsymbol{P}$ is exactly double that of $\boldsymbol{P}_+$. The fundamental sector of $\boldsymbol{P}$ in the "extended" column is not fully enclosed by mirror planes. Direct application of the standard asymmetric HSL distribution will inevitably cause colour discontinuities. To resolve this, the extended asymmetric HSL distribution has been introduced to define discontinuity-free colouring for all symmetry groups $\boldsymbol{P}$ in the "extended" column [48]. The extended asymmetric HSL distribution colours half of the fundamental sector of $\boldsymbol{P}$ to align with that of $\boldsymbol{P}_+$, featuring a bright centre, using the standard asymmetric HSL distribution from the upper unit hemisphere, while the other half is coloured with a dark centre via the standard asymmetric HSL distribution from the lower unit hemisphere. For symmetry groups $\bar{3}$, $\bar{4}$, and $\bar{1}$ listed in the "Exception" column, their fundamental sectors cannot be embedded in three-dimensional space without jumps. Consequently, any IPF distribution of these groups will result in either colour ambiguity or discontinuities. The symmetry group notation in Table 2 adheres to the common convention that is well documented in crystallography textbooks [48].

2.2. Colour to orientation mapping

Synthesised images visualised using the $\boldsymbol{P}$-specific IPF colouring cannot readily specify crystallographic characterisations due to the lack of an inverse mapping from IPF colouring to $\boldsymbol{G}$. This section presents a new mapping method to derive orientations from

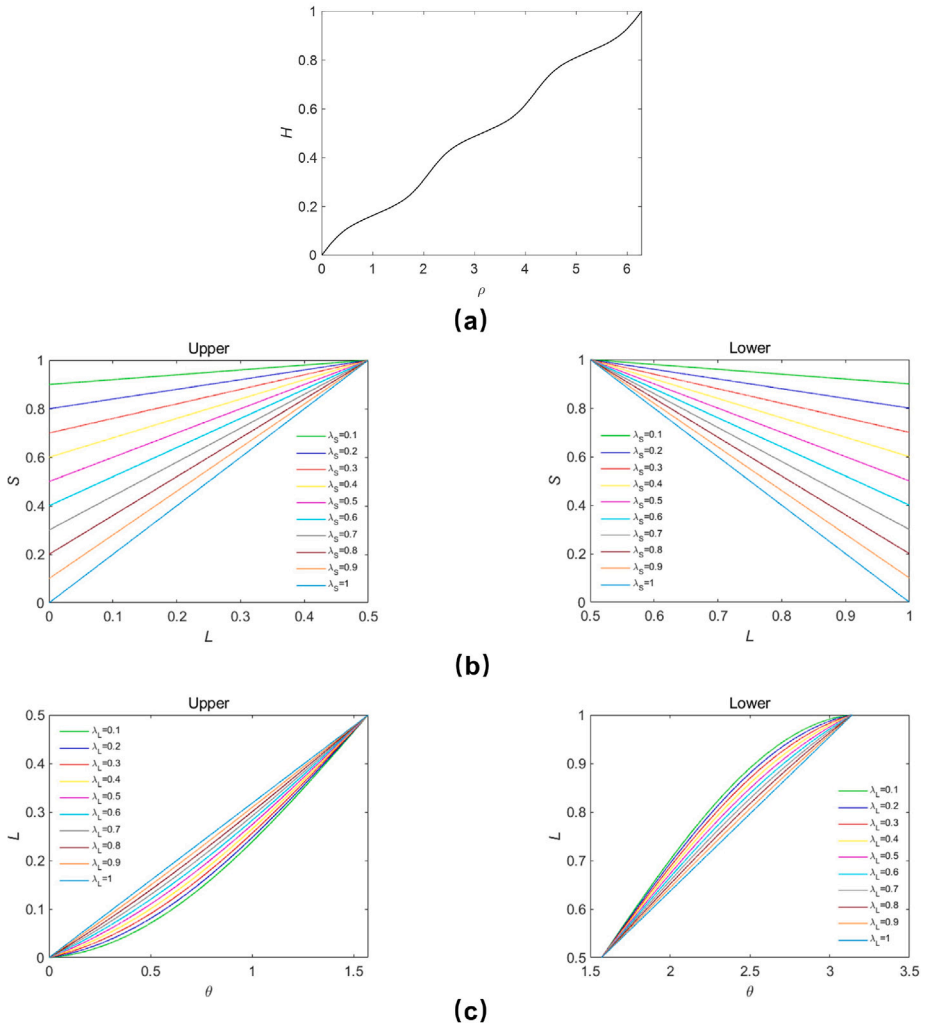

Fig. 3. Precomputed curves: (a) $H-\rho$, (b) $S-L$, and (c) $L-\theta$.

P-specific IPF colouring. This method consists of two key techniques: (1) an inverse IPF colouring to transform RGB triples into azimuthal angle ρ and polar angle θ, and (2) a conditional probability density for azimuthal angle φ (illustrated in Section 2.2.2) to quantify the Rolling Direction (RD) in the specimen coordinate system.

2.2.1. Inverse IPF colouring

The colourmap in standard or extended ***P***-specific IPF colouring establishes a one-to-one mapping between RGB triplets and vector $\boldsymbol{h}$ in the crystal coordinate system (see Eq. (1)). Therefore, the initial step in mapping orientations from the ***P***-specific IPF colouring is converting each RGB triplet into crystal direction $\boldsymbol{h}$. The key steps are summarised below.

- Convert RGB triplets to HSL triplets.
- Calculate ρ from hue H based on Eq. (2). Similarly, calculate θ from lightness L and saturation S based on Eqs. (5) and (6).
- Determine symmetrically equivalent crystal direction $\boldsymbol{h}$ based on θ and ρ.

The relationships between H and ρ in Eq. (2), S and L in Eq. (6), and L and θ in Eq. (5) are monotonic. Therefore, precomputing their function curves can bypass the computationally expensive process of solving these equations, see Fig. 3. The derivation from θ and ρ to $\boldsymbol{h}$ is illustrated in Fig. 4, and the key steps are outlined below.

- Calculate the vector $\boldsymbol{N}_\rho$ perpendicular to the plane P_ρ using conditions (a) $\boldsymbol{N}_\rho \perp \boldsymbol{p}$ and (b) $\boldsymbol{N}_\rho \perp \boldsymbol{b}$, where vector $\boldsymbol{p}$ corresponds to the barycentre p and vector $\boldsymbol{b}$ corresponds to the boundary point b.
- Calculate the vector $\boldsymbol{h}$ via Eq. (7).

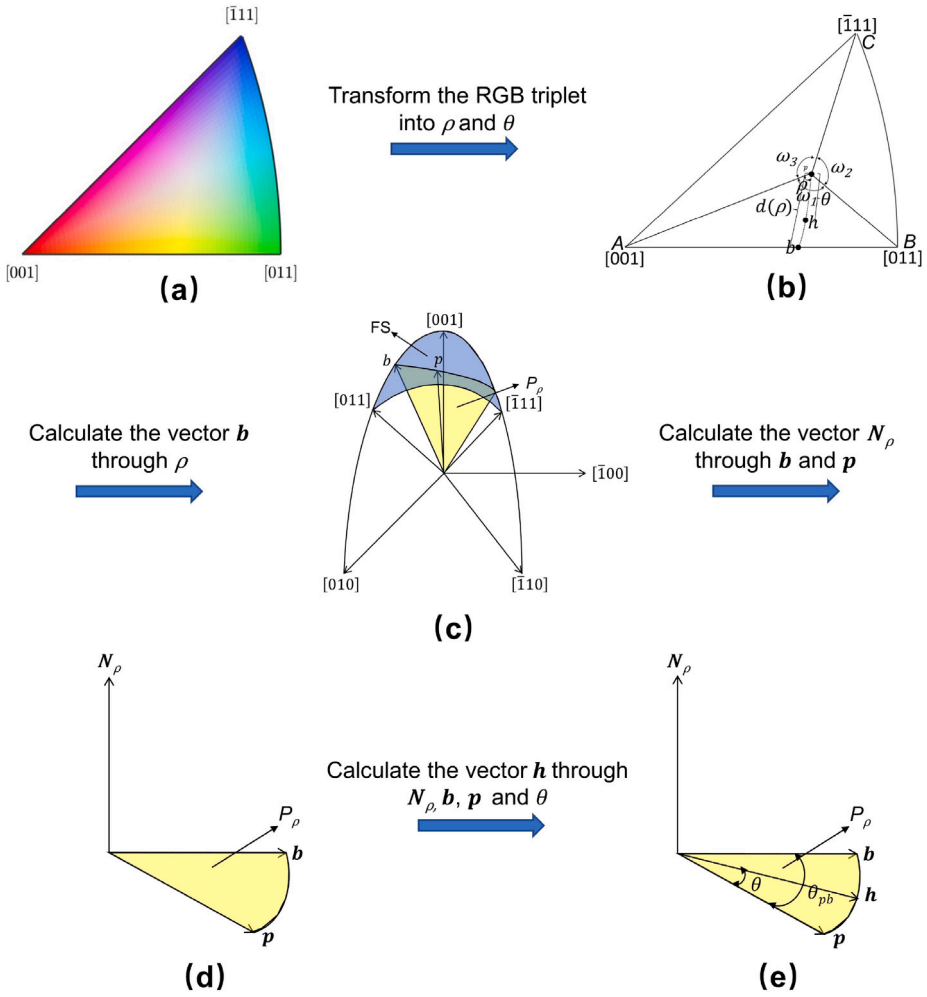

Fig. 4. Flowchart for converting RGB triplet into symmetrically equivalent crystal direction $\boldsymbol{h}$.

$$\begin{aligned} \boldsymbol{h} \cdot \boldsymbol{N}_\rho &= 0 \\ \boldsymbol{h} \cdot \boldsymbol{p} &= cos(\theta) \\ \boldsymbol{h} \cdot \boldsymbol{b} &= cos(\theta_{\rho b}) \end{aligned} \tag{7}$$

where $\cdot$ is the dot product of two vectors, and $\theta_{\rho b}$ is the angle between the vector $\boldsymbol{h}$ and the vector $\boldsymbol{p}$ in the plane P_ρ.

2.2.2. Conditional probability density

Given a crystal direction $\boldsymbol{h}$ corresponding to the normal direction ND, another crystal direction $\boldsymbol{u}$ corresponding to the rolling direction RD can be specified using the azimuthal angle φ. As shown in Fig. 5.a, vector $\boldsymbol{R_1}$ represents the intersection of the plane (010) with the plane P_φ perpendicular to the normal direction ND, and φ is the angle between the vector $\boldsymbol{R_1}$ and the rolling direction RD in the plane P_φ. The calculation of $\boldsymbol{u}$ is shown in Fig. 5.b, and the key steps are summarised below.

- Calculate the vector $\boldsymbol{R_2}$ using conditions (a) $\boldsymbol{R_2} \perp \boldsymbol{h}$ and (b) $\boldsymbol{R_2} \perp \boldsymbol{R_1}$.
- Calculate the vector $\boldsymbol{u}$ (corresponding to the rolling direction RD) via Eq. (8).

$$\begin{aligned} \boldsymbol{u} \cdot \boldsymbol{h} &= 0 \\ \boldsymbol{u} \cdot \boldsymbol{R_1} &= cos(\varphi) \\ \boldsymbol{u} \cdot \boldsymbol{R_2} &= cos(\varphi_1) \end{aligned} \tag{8}$$

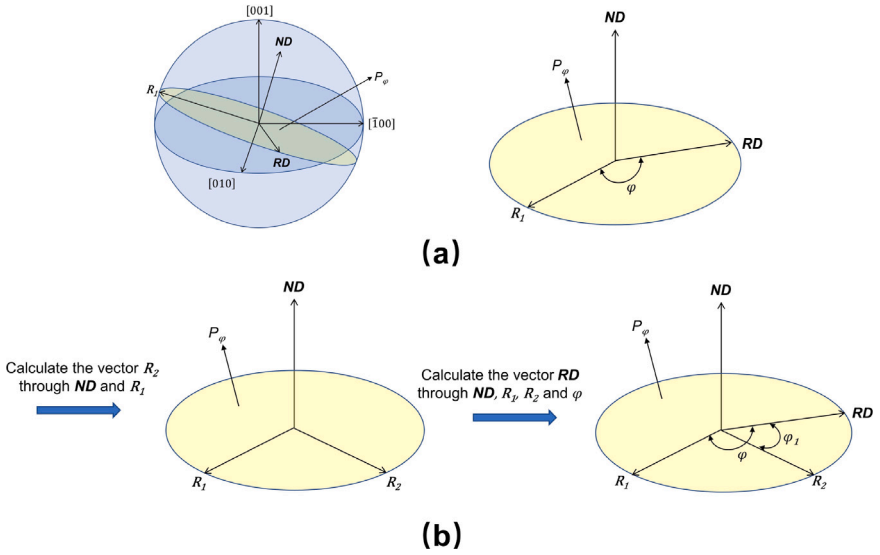

Fig. 5. Illustration of the azimuthal angle φ defined by the vector $\boldsymbol{R_1}$ and the rolling direction RD in the plane P_φ.

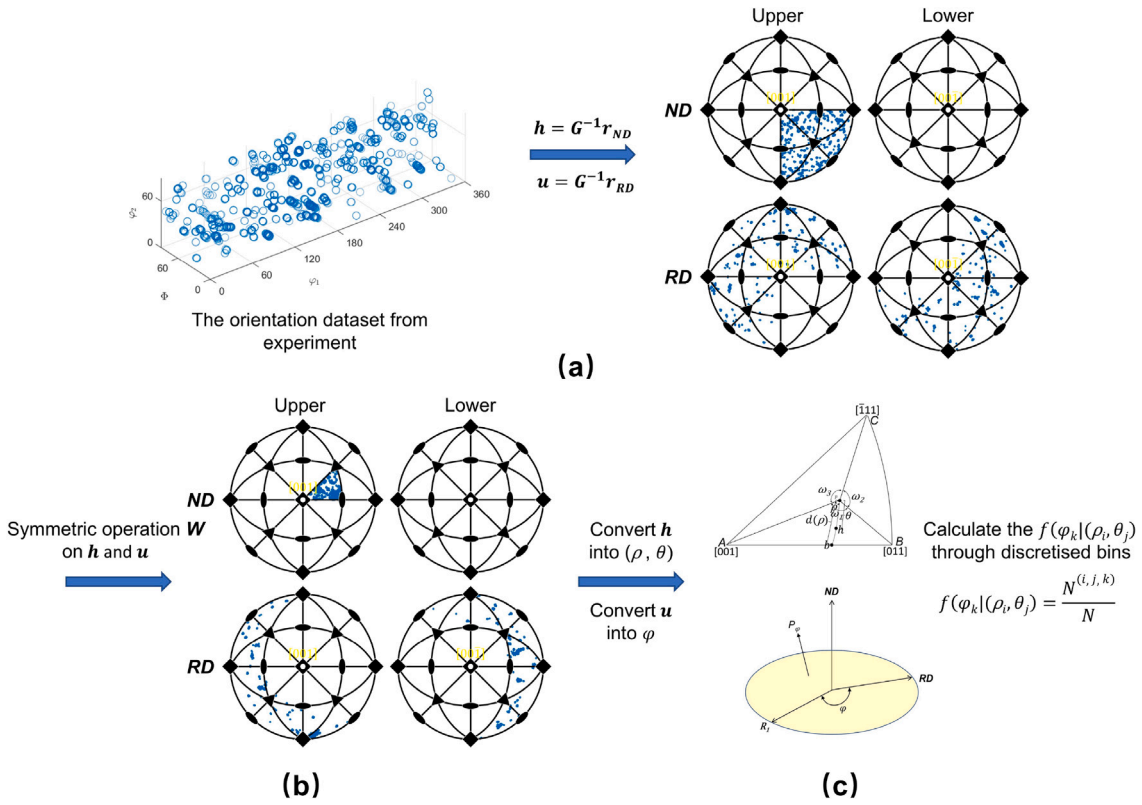

Fig. 6. Illustration of flowchart for calculating $f(\varphi_k|(\rho_i,\ \theta_j))$, using $m\bar{3}m$ symmetry group as example.

where φ_1 is the angle between the vector $\boldsymbol{R_2}$ and the rolling direction RD in the plane P_φ. The relationship between φ_1 and φ is expressed as:

$$\varphi_1 = \begin{cases} \pi/2 - \varphi & 0 \le \varphi < \pi/2 \\ \varphi - \pi/2 & \pi/2 \le \varphi < 3\pi/2 \\ 2\pi - \varphi & 3\pi/2 \le \varphi \le 2\pi \end{cases} \tag{9}$$

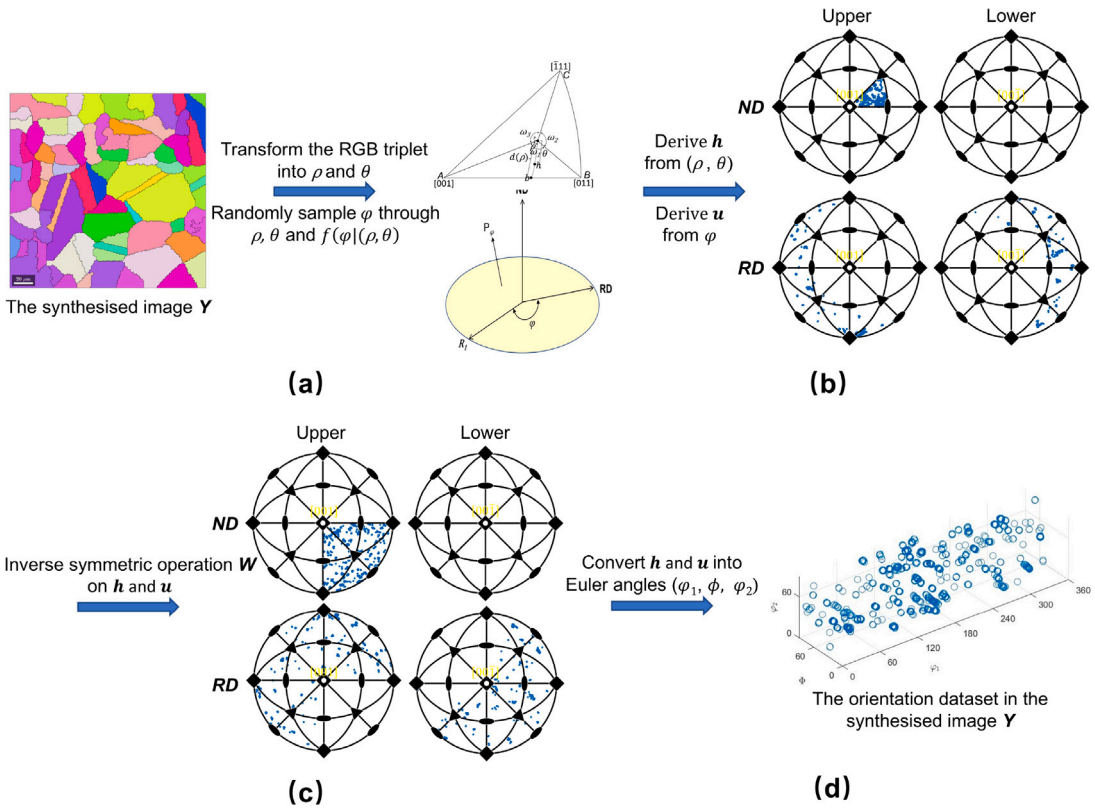

Fig. 7. Illustration of converting RGB triplets into orientation dataset in synthesised image $\boldsymbol{Y}$.

After building the mapping relationship between $\boldsymbol{u}$ and φ, the conditional probability density $f(\varphi_k|(\rho_i,\ \theta_j))$ can be calculated from the orientation dataset, for which the key steps are outlined below.

- Convert the orientation dataset from measurement into crystal directions $\boldsymbol{h}$ and $\boldsymbol{u}$ (see Fig. 6.a).
- Project $\boldsymbol{h}$ onto the fundamental sector via symmetric operation $\boldsymbol{W}$ and apply the same operation to $\boldsymbol{u}$ (see Fig. 6.b).
- Transform $\boldsymbol{h}$ into θ and ρ, while transforming $\boldsymbol{u}$ into φ (see Fig. 6.c).
- Discretise θ, ρ, and φ into bins. For example, ρ ranging from 0° to 360° is divided into I bins ρ_i $(i = 1, 2, \dots, I)$ with bin width $2\pi/I$; θ ranging from 0° to 180° is divided into J bins θ_j $(j = 1, 2, \dots, J)$ with bin width π/J; and φ ranging from 0° to 360° is divided into K bins φ_k $(k = 1, 2, \dots, K)$ with bin width $2\pi/K$.
- Calculate $f(\varphi_k|(\rho_i,\ \theta_j))\ (k = 1, 2, \dots, K) = \frac{N^{(i,\ j,\ k)}}{N}$, where $N^{(i,\ j,\ k)}$ is the number of orientations in $(\rho_i,\ \theta_j,\ \varphi_k)$ element and N is the total number of orientations in elements ranging from $(\rho_i,\ \theta_j,\ \varphi_1)$ to $(\rho_i,\ \theta_j,\ \varphi_K)$.

The Orientation Probability Assignment (OPA) method [51] is applied to randomly sample φ from the conditional probability density $f(\varphi_k|(\rho_i,\ \theta_j))$. Once θ, ρ, and φ are determined (see Fig. 7.a), the reconstructed orientation dataset can be obtained from the synthesised image $\boldsymbol{Y}$. Specifically, $\boldsymbol{h}$ can be calculated from θ and ρ, and $\boldsymbol{u}$ can be derived from φ, as shown in Fig. 7.b-.d. As an example, Fig. 8.a presents the orientation dataset from measurement and Fig. 8.b shows orientation datasets obtained from synthesised images.

3. Image generation from continuous and symmetry-conserved orientation colouring

Section 2 develops novel orientation colour mapping strategies for polycrystalline materials. They include (1) the orientation to colour mapping that enables continuous and symmetry-conserved visualisation of orientation datasets in the form of RGB images; and (2) the colour to orientation mapping that extracts orientation datasets from symmetry-preserved orientation colouring images. Based on these mapping strategies, we propose a novel data-driven digital reconstruction method for polycrystalline microstructures. As shown in Fig. 1, this method comprises four key steps. Step (1) acquires experimental microstructural data, such as lattice symmetry and orientation, from various imaging techniques. For instance, orientation data are acquired at each scan point using orientation microscopy techniques, such as EBSD and X-ray diffraction. Step (2) Converts experimental data into RGB images, using the $\boldsymbol{P}$-specific IPF colouring explained in Section 2.1. The orientation components at each scan point are mapped to the RGB components

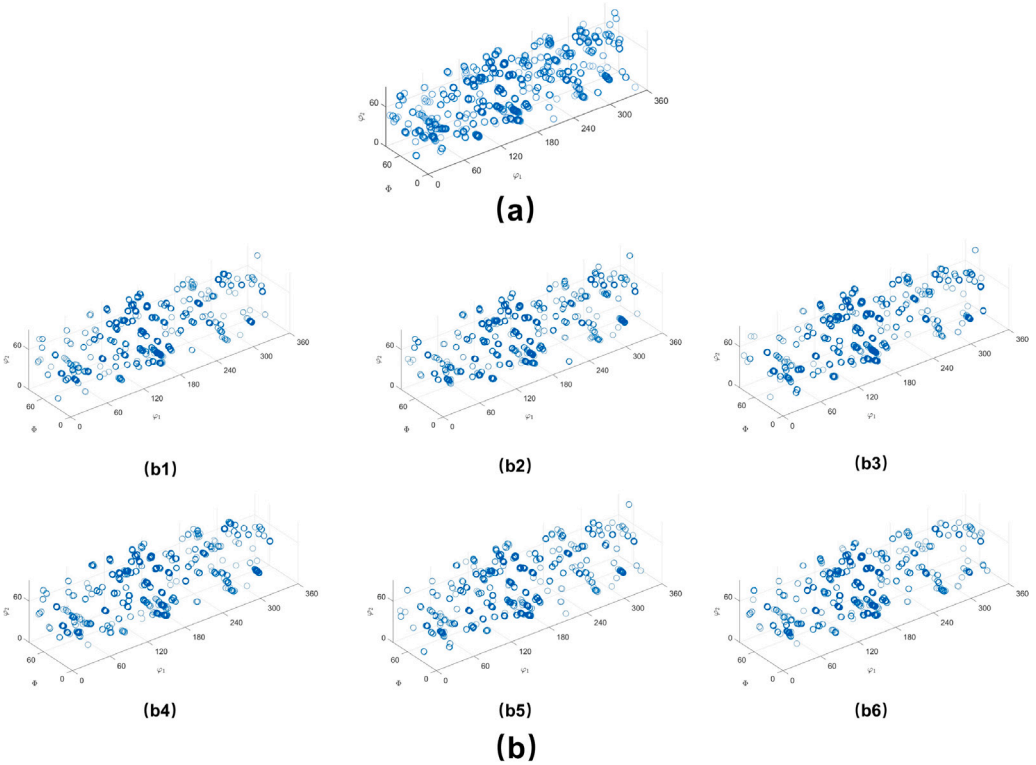

Fig. 8. An example of orientation datasets. (a) The orientation dataset obtained from measurement. (b) The orientation datasets obtained from synthesised images.

of each pixel, meaning that a single pixel represents a single orientation at each scan point. Step (3) generates images using coloured images in Step 2 as reference. The generated images directly represent microstructures of polycrystalline materials and serve as representative volume elements for multiscale simulations. Step (4) reconstructs grain data from synthesised RGB images generated in Step 3, using the colour to orientation mapping explained in Section 2.2.

Recently, image generation algorithms such as texture synthesis [44,45,52,53] and machine learning [46,49] have been employed to reconstruct microstructures of polycrystalline materials. However, these image-based methods have fundamental defects such as discontinuities and ambiguities caused by direct orientation colouring. Furthermore, they only output RGB images for visualisation purposes and do not reconstruct realistic orientation datasets of polycrystalline microstructures.

This section explains step 3, which build polycrystalline images using image generation algorithms. The Patch-based Texture Synthesis (PTS) algorithm with raster-scan order is employed for statistical image generation. Traditionally, fast template matching and image quilting techniques are integrated to preserve microstructural continuity and reduce computational cost.

3.1. Patch-based texture synthesis for polycrystalline microstructures

Texture synthesis has been extensively studied in computer vision, addressing applications such as occlusion filling, image and video compression, and foreground removal. Patch-based Texture Synthesis (PTS), effective in capturing complex features, has been widely applied to reconstructing geological structures [54–56]. We introduce the PTS algorithm for reconstructing polycrystalline materials, and the basic idea of PTS algorithm is illustrated in Fig. 9.

Let $\boldsymbol{X}$ denote the reference image obtained in step 2 and $\boldsymbol{Y}$ denote the synthesised image to be generated in step 3. The PTS algorithm starts at the origin of the raster path in the synthesised domain $\boldsymbol{Y}$, with data event $\boldsymbol{D_T}(\boldsymbol{u})\ \boldsymbol{A}$. A patch $\boldsymbol{T}$ is chosen randomly from the reference image $\boldsymbol{X}$, and inserted into $\boldsymbol{D_T}(\boldsymbol{u})\ \boldsymbol{A}$ at location $\boldsymbol{u}(x, y)$. Then, a small bottom overlap area $\boldsymbol{OL}_b$ is specified (Fig. 9a). The reference image $\boldsymbol{X}$ is scanned for a patch that best matches the overlap area $\boldsymbol{OL}_b$ based on similarity measures. If multiple patches share identical similarities, one is randomly chosen and superimposed into $\boldsymbol{D_T}(\boldsymbol{u})\ \boldsymbol{B}$ alongside the raster path. This procedure is repeated until $\boldsymbol{D_T}(\boldsymbol{u})\ \boldsymbol{C}$ at the end of the first raster path is inserted into a patch from $\boldsymbol{X}$ (Fig. 9b). The PTS algorithm proceeds upward, selecting a raster path adjacent to the previous one. The first patch inserted into $\boldsymbol{D_T}(\boldsymbol{u})\ \boldsymbol{D}$ must match the left overlap area $\boldsymbol{OL}_l$ (Fig. 9c), while the second patch inserted into data event $\boldsymbol{D_T}(\boldsymbol{u})\ \boldsymbol{E}$ must match overlap areas $\boldsymbol{OL}_{lb}$ on the left and bottom sides (Fig. 9d).

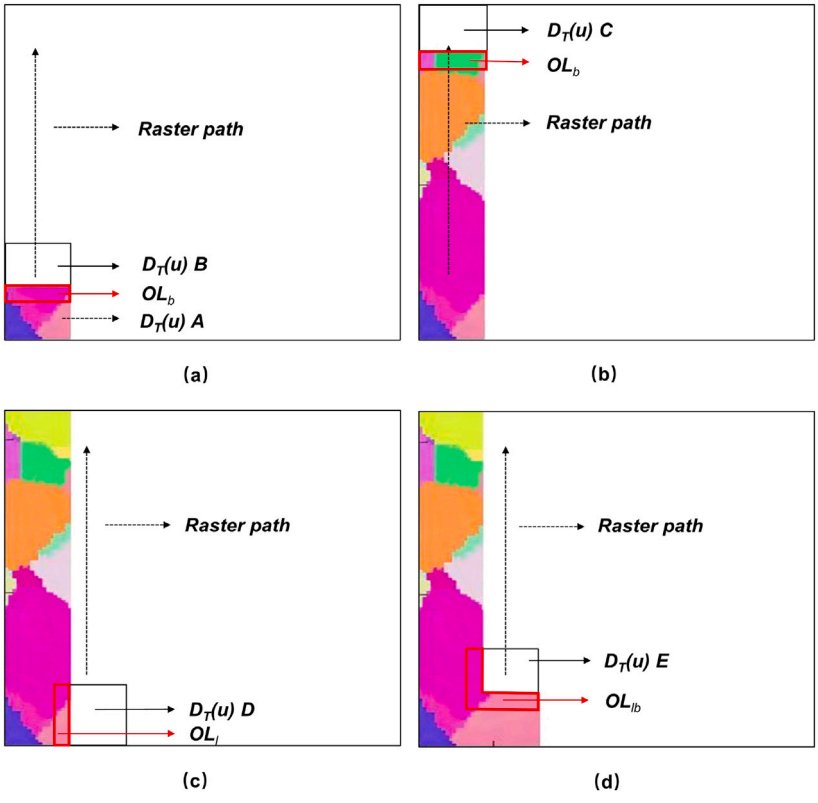

Fig. 9. Illustration of patch-based texture synthesis algorithm with raster-scan order.

Algorithm 1 Algorithm for patch-based texture synthesis

1: **procedure** PTS($\boldsymbol{X}$, $size_{\boldsymbol{T}}$, $size_{\boldsymbol{OL}}$, n_{can}, n_{de})
2: **for** $i = 1 : n_{de}$ **do** ▷ n_{can} is the number of candidates ▷ n_{de} is the number of data events
3: $\boldsymbol{T} \leftarrow randomize\ (size_{\boldsymbol{T}}, \boldsymbol{X})$
4: $\boldsymbol{path} \leftarrow randomize\_raster\ (path\ origin,\ path\ direction)$
5: **for** *each location* $\boldsymbol{u}$ *along* $\boldsymbol{path}$ **do**
6: $\boldsymbol{OL_u} \leftarrow extract\_current\_overlap\ (\boldsymbol{u}, \boldsymbol{T}, size_{\boldsymbol{OL}})$
7: $\boldsymbol{OL_c} \leftarrow template\ matching\ (\boldsymbol{X}, \boldsymbol{OL_u})$ ▷ $\boldsymbol{OL_c}$ are candidate overlap regions
8: $\boldsymbol{cand\_loc} \leftarrow extract\_candidate\_locations\ (\boldsymbol{OL_c}, n_{can})$
9: $\boldsymbol{loc} \leftarrow randomize\ (\boldsymbol{cand\_loc})$ ▷ $\boldsymbol{cand\_loc}$ are candidate locations in $\boldsymbol{X}$
10: $\boldsymbol{D_T(u)} \leftarrow assign\ (\boldsymbol{loc}, \boldsymbol{X}, size_{\boldsymbol{T}})$
11: **end for**
12: **end for**
13: **return** all data events $\boldsymbol{D_T(u)}$
14: **end procedure**

The pseudo-code for the PTS method is provided in Algorithm 1. Inputs required for the PTS algorithm include reference image $\boldsymbol{X}$, patch size $\boldsymbol{T}$, and overlap region size $\boldsymbol{OL}$. Random raster path origin, direction, patch location in $\boldsymbol{X}$, and patch size ensure sufficient stochastic realisations (lines 3–4). The template matching function is calculated from the overlap region $\boldsymbol{OL}$ of each data event $\boldsymbol{D_T(u)}$ along the raster path, and it measures the similarity between overlap region $\boldsymbol{OL}$ and reference image $\boldsymbol{X}$ (lines 6–7). The three RGB channels can be processed in parallel in the template matching algorithm (line 7) to generate a unified matching location in $\boldsymbol{X}$. Implementing template matching using the greyscale channel is a simple and effective approach. Candidate locations $\boldsymbol{cand\_loc}$, corresponding to overlap candidate regions $\boldsymbol{OL_c}$, are then extracted from $\boldsymbol{X}$ (line 8). A random location is selected, and the patch at that location is assigned to data event $\boldsymbol{D_T(u)}$ at location $\boldsymbol{u}(x, y)$ (lines 9–10). The algorithm continues along the raster paths, repeating the process until all data events $\boldsymbol{D_T(u)}$ are assigned patches (line 11).

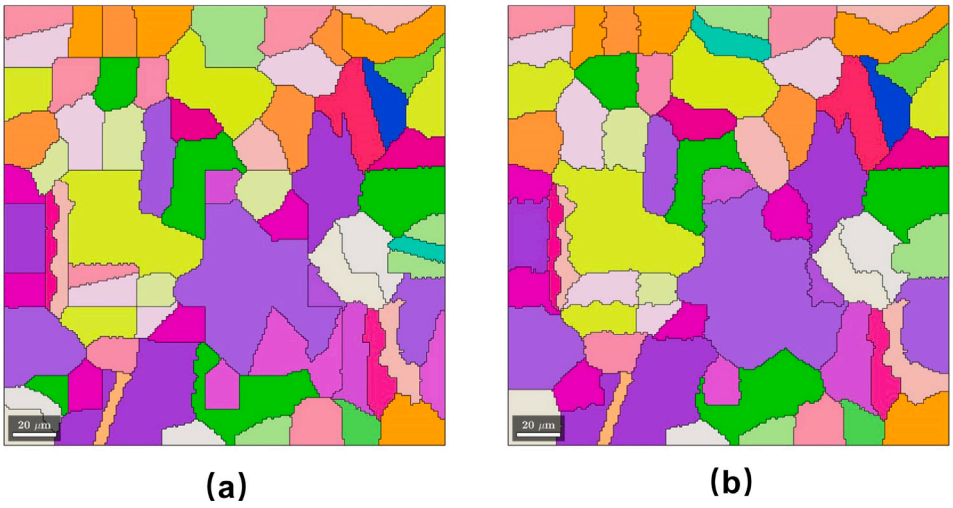

Fig. 10. Illustration of imaging quilting algorithm: (a) patch-based texture synthesis without imaging quitting; (b) patch-based texture synthesis with imaging quitting.

3.2. Fast template matching

The cross-correlation template matching approach substantially improves simulation speed and patch reproduction [55]. Functioning as a filtering template via convolution, cross-correlation efficiency can be further enhanced using convolution theorem [56], described as:

$$\boldsymbol{X} \otimes \boldsymbol{OL} = \mathfrak{F}^{-1}\left[\mathfrak{F}(\boldsymbol{X}) * \mathfrak{F}(\boldsymbol{OL})\right] \tag{10}$$

where $\otimes$ indicates the convolution between $\boldsymbol{X}$ and $\boldsymbol{OL}$, $*$ denotes the pointwise product operation, $\mathfrak{F}$ and $\mathfrak{F}^{-1}$ represent the Fourier transform and inverse Fourier transform, respectively. The Fourier transform of the convolution between $\boldsymbol{X}$ and $\boldsymbol{OL}$ equals the pointwise product of the Fourier transforms of $\boldsymbol{X}$ and $\boldsymbol{OL}$. Thus, the improved template match algorithm entails converting $\boldsymbol{X}$ and $\boldsymbol{OL}$ to the frequency domain via the fast Fourier transform, expressed as:

$$\mathfrak{F}\left[f(x,y)\right] = F(u,v) = \sum_{x=0}^{I-1}\sum_{y=0}^{J-1} exp\left[-2\pi i(ux/I + vy/J)\right] \tag{11}$$

where $f(x,y)$, for $x = 0,1,2,\ldots,I-1$, and $y = 0,1,2,\ldots,J-1$, indicates an $I \times J$ image in the spatial domain. Subsequently, the pointwise product of the Fourier transforms of $\boldsymbol{X}$ and $\boldsymbol{OL}$ is computed, and the inverse Fourier transform converts the result into the spatial domain, expressed as:

$$f(x,y) = \frac{1}{I \times J}\sum_{u=0}^{I-1}\sum_{v=0}^{J-1} F(u,v)exp\left[2\pi i(ux/I + vy/J)\right] \tag{12}$$

3.3. Image quilting

Fig. 10 presents synthesised results using the PTS method. Vertical and horizontal incompatibilities are evident at the edges of overlapping patches (see Fig. 10.a). Noticeable seams in overlap areas disrupt grain boundary structures. These inconsistencies arise from significant overlap errors due to suboptimal patch selection. To address this, the imaging quilting algorithm [57–61] is integrated into the PTS model. The image quilting algorithm evaluates overlap errors between the selected patch in reference $\boldsymbol{X}$ and the patch in $\boldsymbol{D_T(u)}$ to obtain a minimum cost path that redefines boundaries in overlap areas. Fig. 10.b shows results from the image quilting algorithm, demonstrating its ability to significantly improve patch continuity and better capture boundary features in polycrystalline materials.

The pseudocode in Algorithm 2 computes the minimum cost path for a vertical overlap area. Input parameters are two overlapping patches, $\boldsymbol{T}_1$ and $\boldsymbol{T}_2$, with overlap areas $\boldsymbol{OL}_1$ and $\boldsymbol{OL}_2$. This algorithm begins by identifying the surface error $\boldsymbol{e}$ as the smallest squared distance between $\boldsymbol{OL}_1$ and $\boldsymbol{OL}_2$ (line 2). Cumulative minimum error $\boldsymbol{E}$ is computed along the vertical direction (lines 3–9). The smallest value in the last row of $\boldsymbol{E}$ indicates the final minimum cost path arrival point k. The arrival point k for each row i ($i = n-1,\ldots,1$) is traced back as $min\ (\boldsymbol{E}_{i,k-1},\ \boldsymbol{E}_{i,k},\ \boldsymbol{E}_{i,k+1})$ to determine the minimum cost path (lines 10–11). The same

Algorithm 2 Algorithm for image quilting

procedure PTS ($\boldsymbol{T}_1$, $\boldsymbol{T}_2$, $\boldsymbol{OL}_1$, $\boldsymbol{OL}_2$)
  $\boldsymbol{e} \leftarrow (\boldsymbol{OL}_1 - \boldsymbol{OL}_1)^2$
  for $i = 1 : m$ **do** ▷ m is the row number in $\boldsymbol{e}$
    for $j = 1 : n$ **do** ▷ n is the column number in $\boldsymbol{e}$
      $\boldsymbol{E}_{i,j} \leftarrow \boldsymbol{e}_{i,j} + min\ (\boldsymbol{E}_{i-1,j-1},\ \boldsymbol{E}_{i-1,j},\ \boldsymbol{E}_{i-1,j+1});\ if\ j = 2, ..., n-1$
      $\boldsymbol{E}_{i,j} \leftarrow \boldsymbol{e}_{i,j} + min\ (\boldsymbol{E}_{i-1,j},\ \boldsymbol{E}_{i-1,j+1});\ if\ j = 1$
      $\boldsymbol{E}_{i,j} \leftarrow \boldsymbol{e}_{i,j} + min\ (\boldsymbol{E}_{i-1,j-1},\ \boldsymbol{E}_{i-1,j});\ if\ j = n$
    end for
  end for
  $k \leftarrow min\ (\boldsymbol{E}_{m,j});\ j = 1, ..., n$ ▷ k denotes the arrival point of MCP on the last row of $\boldsymbol{E}$
  $MCP \leftarrow min\ (\boldsymbol{E}_{i,k-1},\ \boldsymbol{E}_{i,k},\ \boldsymbol{E}_{i,k+1});\ i = n-1, ..., 1$
end procedure

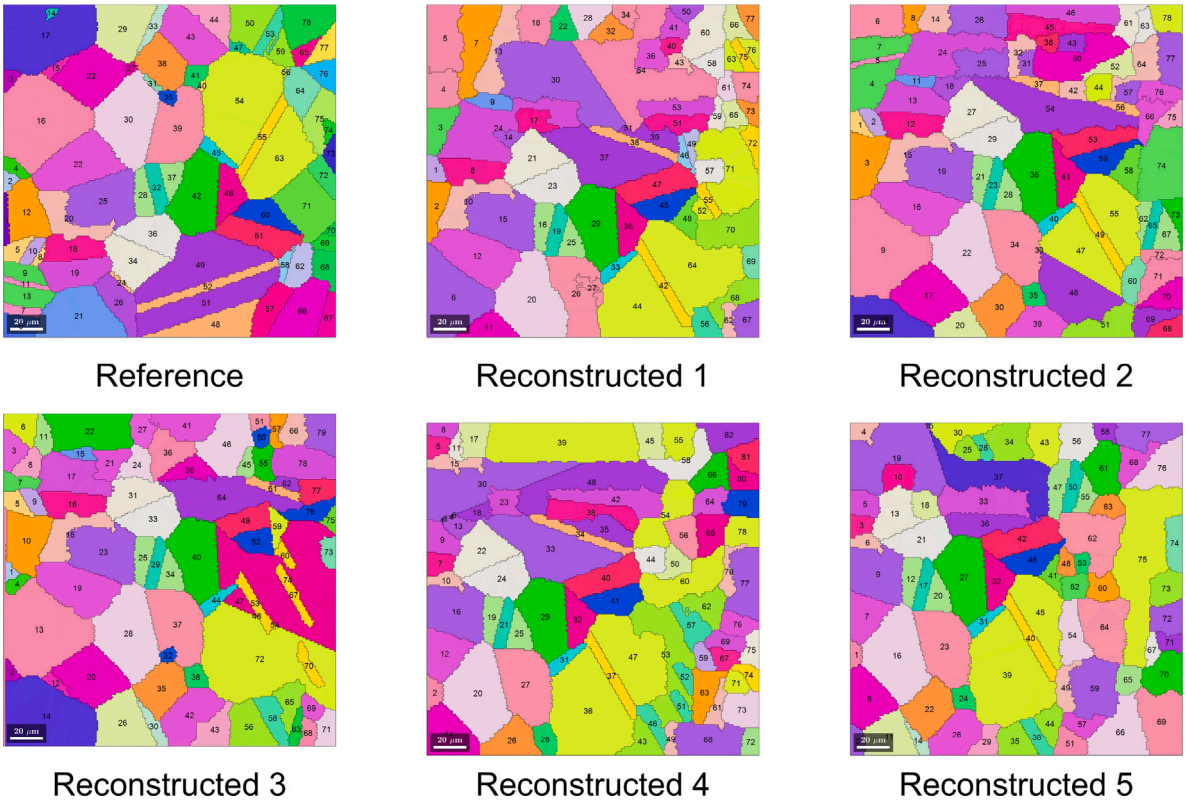

Fig. 11. Illustration of data-driven polycrystalline microstructure reconstruction.

principle applies to the minimum cost path computation for horizontal overlap areas.

4. Example and application

In this section, we use Inconel 718 nickel superalloy [62–65] (IN718) to examine the performance of the proposed data-driven digital reconstruction method for polycrystalline microstructures, and demonstrates its use in crystal plasticity simulation to study the mechanical properties of the material.

4.1. Performance examination

An IN718 sample was prepared with grinding and polishing, and its lattice orientation was measured by EBSD [63] (step 1 in Fig. 1). Then, using the orientation to colour mapping explained in Section 2.1, the orientation data was converted into RGB values to

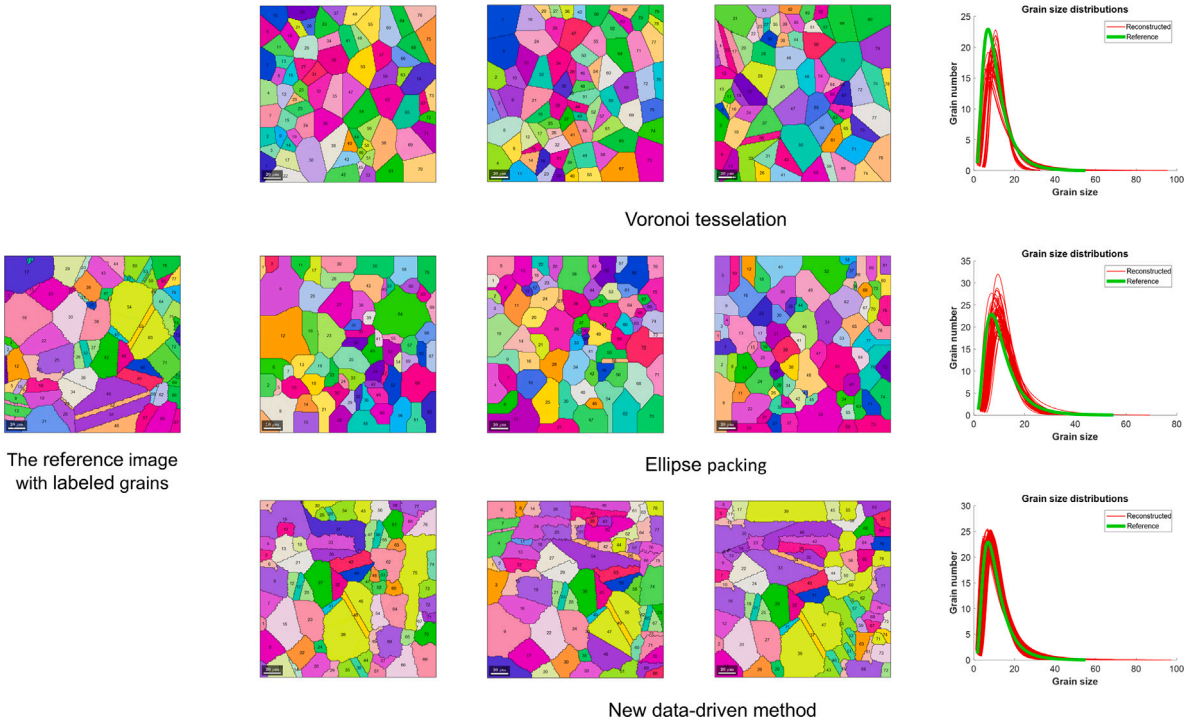

Fig. 12. Comparison of polycrystalline material reconstruction between Voronoi tessellation, ellipse packing, and the new data-driven method.

form the reference image (step 2 in Fig. 1). Next, synthesised images were generated using the PTS algorithm explained in Section 3 (step 3 in Fig. 1). Finally, using the colour to orientation mapping explained in Section 2.2, the synthesised images were converted into orientation data to form grain microstructures (step 4 in Fig. 1). Fig. 11 illustrates the reconstruction, including the reference data and five reconstructed examples.

We further validate the proposed data-driven reconstruction method by comparing it with Voronoi tessellation and ellipse packing methods through morphological parameters of grains. The details of the methodology for establishing the morphological parameters of grains are provided in Appendix A. Reconstructed microstructures and grain size distributions generated by Voronoi tessellation, ellipse packing, and the data-driven method are shown in Fig. 12. The data-driven method outperforms Voronoi tessellation and ellipse packing in grain boundary characterisation, especially for twin boundaries. Meanwhile, Voronoi tessellation significantly underestimates grain size distribution. Although ellipsoid packing outperforms Voronoi tessellation, it slightly overestimates grain size distribution. The novel data-driven reconstruction approach perfectly matches the grain size distribution observed in the reference polycrystalline microstructure. Fig. 13 show the grain orientation distributions (see Appendix A) for reference and reconstructed polycrystalline microstructures. The grain orientation distribution of the reconstructed polycrystalline microstructures is statistically equivalent to those of the reference microstructure.

4.2. Crystal plasticity simulation

In recent years, extensive studies have been conducted to correlate microstructure characteristics with micromechanical properties in polycrystalline materials. Ductile failure is the most critical failure mode for IN718 superalloy. This section presents a case study that integrates the proposed data-driven polycrystalline microstructure reconstruction method with crystal plasticity finite element simulation [66–70]. The simulation is implemented as a user-material (UMAT) subroutine in the commercial finite element software package ABAQUS to investigate the structure–property linkage of the IN718 nickel superalloy.

Table 3 summarises the material properties for IN718 used in this study. Elastic parameters of a single crystal including Young's modulus E, shear modulus G and Poisson ratio ν are taken from [71]. For the same single crystal, its plastic parameters are calibrated through an unconfined micropillar compression test, as shown in Fig. 14. The top row of Fig. 14 presents the unconfined compression tests on three single-crystal micropillars with varying strain rates (10^{-4} s^{-1}, 10^{-3} s^{-1}, 10^{-2} s^{-1}) and loading directions ($\langle 235 \rangle$, $\langle 235 \rangle$, $\langle 213 \rangle$). A single-crystal plasticity finite element model was implemented in order to match the experimental results. The element type is an eight-node brick element (C3D8), and the boundary and loading conditions are configured to represent uniaxial compression. One end of the specimen is fixed in all directions, while a displacement is applied in the axial (compressive) direction at the opposite end. The middle row of Fig. 14 shows the deformed micropillar shape and slip band locations are accurately captured by the simulations. The bottom row of Fig. 14 compares the simulated stress–strain curves (dashed black line) with the experimental results

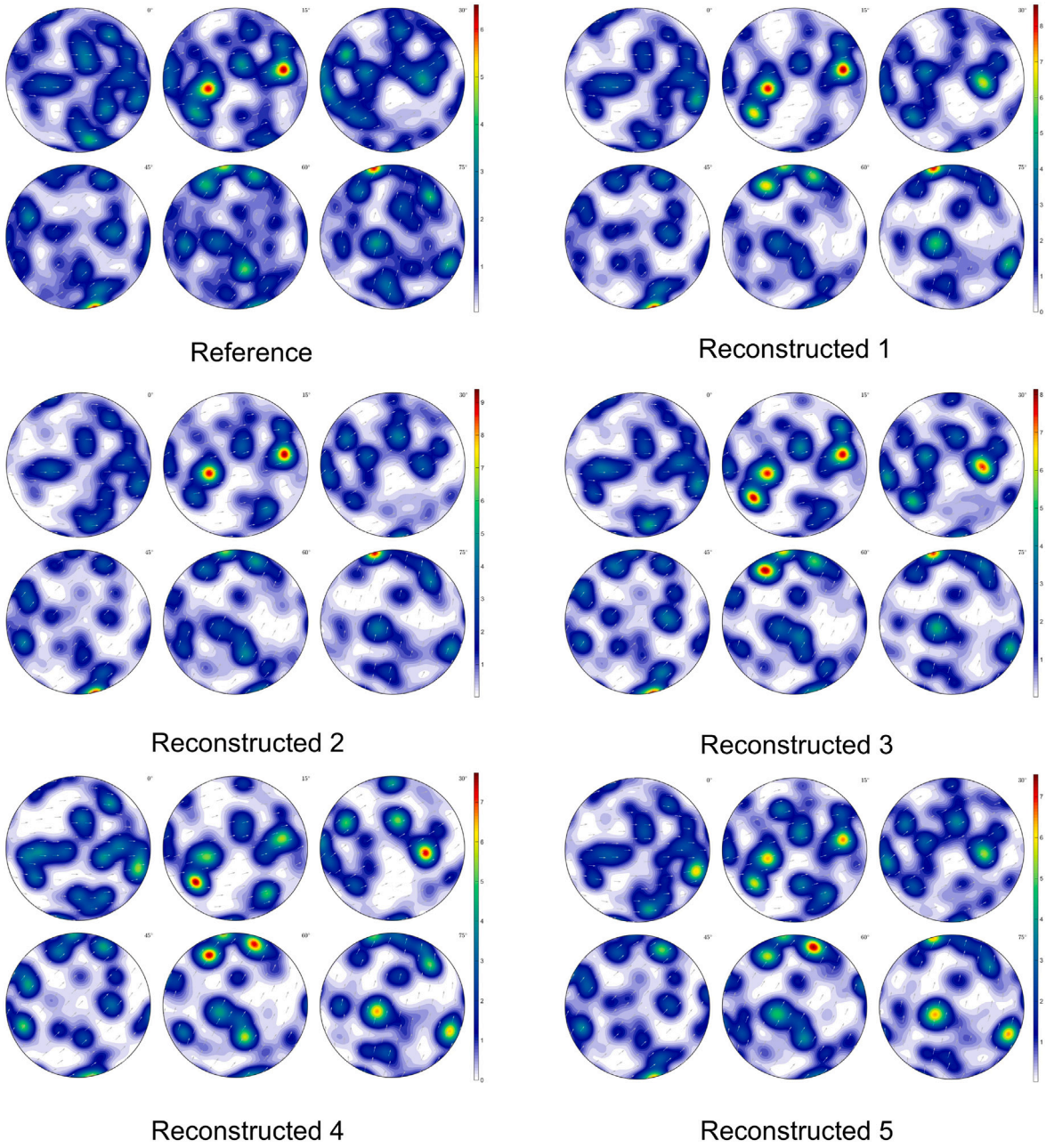

Fig. 13. Illustration of grain orientation distributions in reference and reconstructed microstructures.

(solid red line). By matching the single-crystal plasticity finite element simulation with the unconfined micropillar compression tests, the plastic parameters ($\dot{\gamma}_0$, S_0 and others) used in this study are determined.

To demonstrate the application of the proposed data-driven polycrystalline microstructure reconstruction method, we reconstructed five IN718 polycrystalline RVEs (as shown in Fig. 11) and conducted crystal plasticity finite element analysis. In the RVE simulation, each pixel in the reconstructed images corresponds to an eight-node brick element (C3D8). The grain properties are set according to Table 3, and the boundary and loading conditions are configured to represent uniaxial tension. One end of the RVE is fixed in all directions, while a displacement is applied in the axial (tensile) direction at the opposite end. The accumulated equivalent plastic strain model [67] is adopted to represent ductile failure. The reconstructed polycrystalline RVEs under uniaxial tension exhibit softening behaviour during damage evolution, with over-softening occurring if damage initiates prematurely or progresses too rapidly. To mitigate this issue in crystal plasticity finite element simulations, appropriate thresholds for damage initiation are imposed, and a modified local elastic stiffness tensor is implemented to account for the reduced load-carrying capacity

Table 3
Material properties of IN718 nickel superalloy used in crystal plasticity finite element simulation.

Classification	Name	Symbol	Unit	Value
Elastic	Young's modulus	E	GPa	113.494
	Shear modulus	G	GPa	109.6
	Poisson ratio	ν	–	0.408
Plastic	Reference plastic strain rate	$\dot{\gamma}_0$	s^{-1}	450
	Total free energy required to overcome the lattice resistance	F_0	kJ mol^{-1}	286
	Exponential constant related to material plastic property	p	–	1.0
	Exponential constant related to material plastic property	q	–	1.9
	Lattice friction stress at $0K$	τ_0	MPa	781.3
	Initial slip resistance	S_0	MPa	2.04
	Saturated slip resistance	S_{sat}	MPa	5529.95
	Material constant	h_s	MPa	330.0
	Hardening parameter of the material	w_0	–	1
	Hardening parameter of the material	w_1	–	1

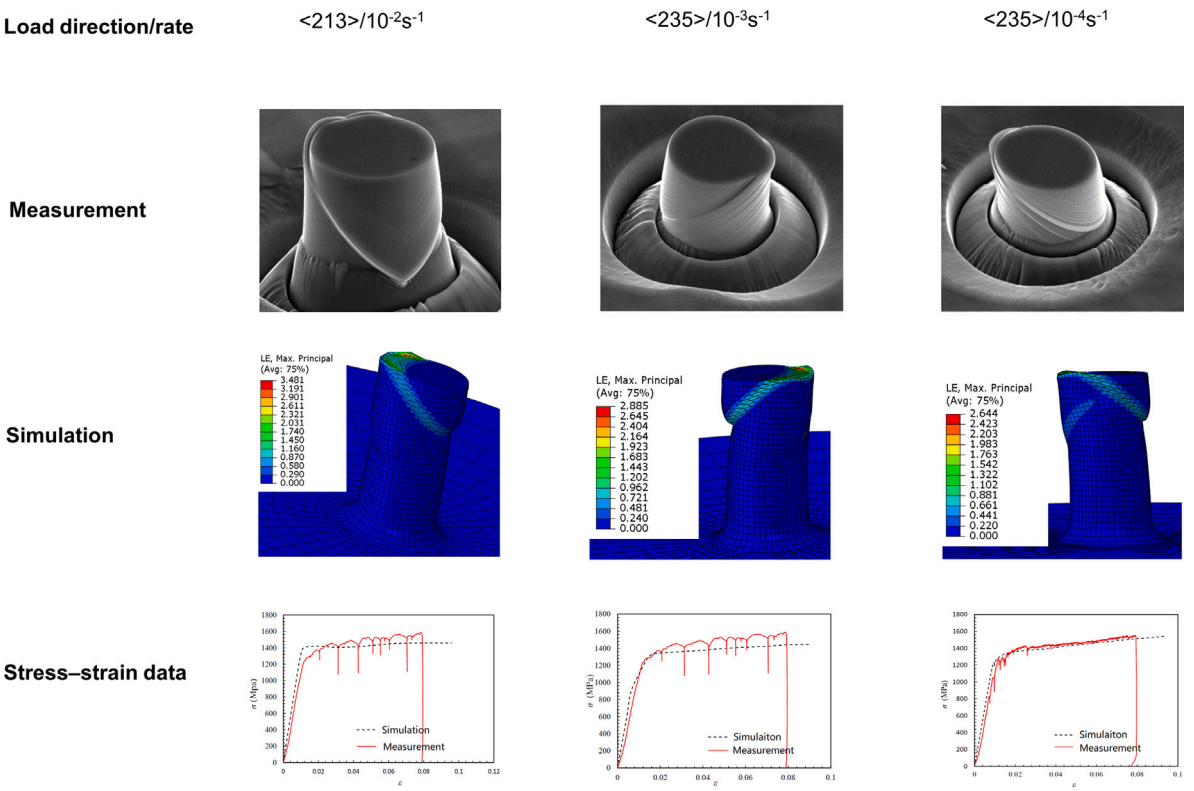

Fig. 14. Stress–strain data from experimental measurements and CPFEM simulations of unconfined compression tests on single crystal micropillars. (For interpretation of the references to colour in this figure legend, the reader is referred to the web version of this article.)

due to damage (see Appendix B for details). Fig. 15 shows the stress–strain curves obtained from RVE simulations, where the red lines are results from the reconstructed RVEs and the green line is the result from the reference RVE. Homogenised stress $\langle\sigma\rangle$ is calculated by averaging von Mises stresses σ_M^i across the computational domain:

$$\langle\sigma\rangle = \frac{1}{N}\sum_{i=1}^{N}\sigma_M^i \tag{13}$$

where N denotes the number of elements in the computational domain. Engineering strain is calculated as:

$$\varepsilon = \frac{L - L_0}{L_0} \tag{14}$$

where L_0 and L represent the initial and current lengths along the tensile axis. Corresponding to the stress–strain curve results shown in Fig. 15, the ductile damage locations are presented in Fig. 16. Based on Figs. 15 and 16, it can be inferred that microstructural variability within RVEs significantly affects the stress–strain response and the localisation of ductile damage in polycrystalline

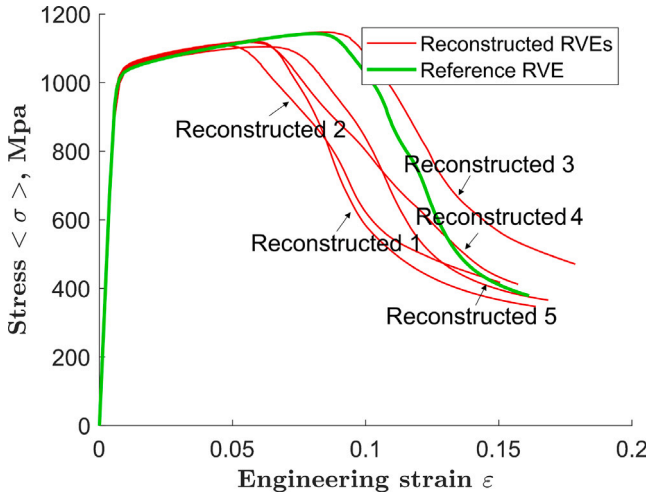

Fig. 15. Stress–strain curves obtained from RVE simulations of IN718. (For interpretation of the references to colour in this figure legend, the reader is referred to the web version of this article.)

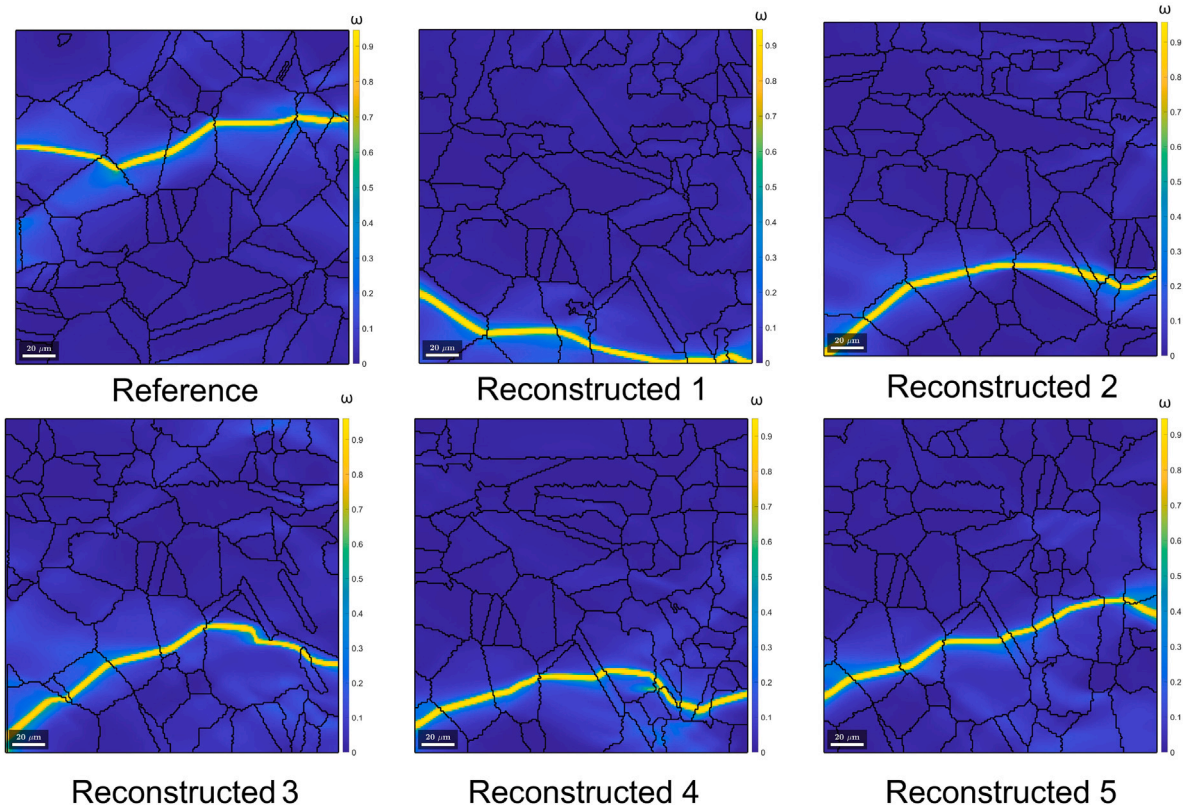

Fig. 16. Ductile damage (ω) locations obtained from RVE simulations of IN718.

materials. Specifically, factors such as grain size, orientation, and boundaries play a crucial role in determining strength, ductility, and the initiation and propagation of damage.

5. Conclusions and future work

This study presents a novel data-driven digital reconstruction method for polycrystalline materials. The orientation-colour mapping strategies not only intuitively visualise polycrystalline microstructures without discontinuity or inconsistency issues, but

they also enable the generation of orientation datasets from synthesised polycrystalline images that share the same statistical features as the reference microstructure. Directly guided by the orientation dataset obtained from measurement, the proposed data-driven digital reconstruction method enables efficient microstructure generation with high fidelity to capture comprehensively the morphological and crystallographic features of polycrystalline materials. The new method provides a powerful tool to work with crystal plasticity finite element analysis for studying the structure–property linkage of alloy materials. Although this study focuses on the two-dimensional case, the new data-driven digital reconstruction method can be extended to three dimensions. While the method is explained using a face centred cubic structure, the proposed method can be readily applied to various polycrystalline materials with different symmetry groups.

CRediT authorship contribution statement

Bingbing Chen: Writing – original draft, Methodology, Investigation, Formal analysis. **Dongfeng Li:** Validation, Methodology, Conceptualization. **Liyuan Wang:** Visualization, Data curation. **Xiangyun Ge:** Visualization, Data curation. **Chenfeng Li:** Writing – review & editing, Supervision, Software, Resources, Project administration, Funding acquisition, Conceptualization.

Declaration of competing interest

The authors declare the following financial interests/personal relationships which may be considered as potential competing interests: Chenfeng Li reports financial support was provided by The Royal Society. Dongfeng Li reports financial support was provided by National Natural Science Foundation of China. If there are other authors, they declare that they have no known competing financial interests or personal relationships that could have appeared to influence the work reported in this paper.

Acknowledgements

The authors would like to thank the supports from Chinese Scholarship Council, Swansea University, and the Royal Society, United Kingdom (IF\R2\23200112, IEC\NSFC\191628).

Appendix A. Grain size distribution and orientation distribution function

In polycrystalline materials, morphological characteristics such as grain size, volume, topology, and neighbourhood provide essential statistical data for grain-level analysis. Recent studies highlight a strong correlation between Grain Size Distribution (GSD) and distributions of grain volume, topology, and neighbourhoods [5,72], and GSD is widely employed to validate RVEs generated through geometry-based methods. The GSD is expressed as:

$$\int_0^{\infty} f(r)dr = \int_0^{r_{max}} f(r)dr = 1, \quad p(a \le r \le b) = \int_a^b f(r)dr \tag{A.1}$$

where $f(r)dr$ represents the number fraction of grains within a size range of $r - \frac{dr}{2} \le r < r + \frac{dr}{2}$, r is the grain size specified by the equivalent circle radius, computed as:

$$r = \left(\frac{1}{4\pi} S_{grain}\right)^{\frac{1}{2}} \tag{A.2}$$

where S_{grain} is the grain area. GSD often exhibits a log-normal distribution [5,72], expressed as:

$$f(r) = \frac{b}{\sqrt{\pi} r} e^{\left[-b^2\left\{ln\left(\frac{r}{r_m}\right)\right\}^2\right]} \tag{A.3}$$

where b denotes a constant and r_m represents median grain size. Crystallographic characterisations in polycrystalline materials are typically evaluated through the Orientation Distribution Function (ODF), which defines grains' preferred crystallographic orientations [73], expressed as:

$$f(\boldsymbol{g})d\boldsymbol{g} = \frac{V_{\boldsymbol{G}\pm\frac{d\boldsymbol{G}}{2}}}{V}, \quad \int_{\boldsymbol{g}\in\boldsymbol{G}} f(\boldsymbol{g})d\boldsymbol{g} = 1 \tag{A.4}$$

where $\boldsymbol{G}$ is the orientation space, and $\frac{V_{\boldsymbol{G}\pm\frac{d\boldsymbol{G}}{2}}}{V}$ denotes the volume fraction associated with orientation $\boldsymbol{g}$ lying within an invariant measure $d\boldsymbol{g}$. ODF is commonly visualised using stereographic projections.

Appendix B. Ductile failure model

Damage initiation and propagation in ductile metals are closely related to the accumulated equivalent plastic strain ε_{eq} defined as [67]:

$$\varepsilon_{eq} = \int_0^t \left(\frac{2}{3}\boldsymbol{D}^p : \boldsymbol{D}^p\right)^{\frac{1}{2}} dt \tag{B.1}$$

where t denotes the current time, and the symmetric part of the plastic velocity gradient gives the plastic strain rate $\boldsymbol{D}^p$ as:

$$\begin{aligned}\boldsymbol{D}^p &= \frac{1}{2}(\boldsymbol{L}^{p*} + (\boldsymbol{L}^{p*})^T) \\ &= \frac{1}{2}(\boldsymbol{F}^e \boldsymbol{L}^p (\boldsymbol{F}^e)^{-1} + (\boldsymbol{F}^e)^{-T}(\boldsymbol{L}^p)^T (\boldsymbol{F}^e)^T) \\ &= \frac{1}{2}\sum_{\alpha=1}^{N} \dot{\gamma}^\alpha \left[\boldsymbol{F}^e \boldsymbol{m}^\alpha \otimes \boldsymbol{n}^\alpha (\boldsymbol{F}^e)^{-1} + (\boldsymbol{F}^e)^{-T}\boldsymbol{n}^\alpha \otimes \boldsymbol{m}^\alpha (\boldsymbol{F}^e)^T\right]\end{aligned} \tag{B.2}$$

where $\boldsymbol{L}^{p*} = \boldsymbol{F}^e \boldsymbol{L}^p (\boldsymbol{F}^e)^{-1}$ stands for the plastic velocity gradient in the final configuration, and $\boldsymbol{L}^p$ refers to the plastic velocity gradient in the intermediate configuration.

A strain-controlled variable ω is introduced to account for damage, where material damage occurs when threshold plastic strain ε_c is reached. Variable ω is 0 for no damage and 1 for total damage. Thus, the damage criterion is expressed as:

$$\omega = \begin{cases} 0, & if\ \varepsilon_{eq} < \varepsilon_c \\ 1, & otherwise \end{cases} \tag{B.3}$$

A modified local elastic stiffness tensor $\mathfrak{T}^*$ is employed to represent reduced load-carrying ability due to damage, given as:

$$\mathfrak{T}^* = \mathfrak{T}(1-\omega) \tag{B.4}$$

An abrupt change in ω value within finite element models can lead to significant fluctuations in the local stress state, making it challenging to achieve equilibrium. Therefore, a modified Cauchy–Lorentz cumulative distribution function is introduced to represent a continuously varying ω as:

$$\omega = 1 + \left[\frac{1}{2} + \frac{1}{\pi}arctan(\frac{\varepsilon_c}{d})\right]^{-1}\left[\frac{1}{\pi}arctan(\frac{\varepsilon_{eq}-\varepsilon_c}{d}) - \frac{1}{2}\right] \tag{B.5}$$

A nonzero value of d enables a smooth transition from $\omega = 0$ to $\omega = 1$. In this work, d is set to 0.1.

Data availability

No data was used for the research described in the article.

References

[1] S.A.H. Motaman, C. Haase, The microstructural effects on the mechanical response of polycrystals: A comparative experimental-numerical study on conventionally and additively manufactured metallic materials, Int. J. Plast. 140 (2021) 102941, https://doi.org/10.1016/j.ijplas.2021.102941.
[2] J. Błachnio, J. Spychała, D. Zasada, Analysis of structural changes in a gas turbine blade as a result of high temperature and stress, Eng. Fail. Anal. 127 (2021) 105554, https://doi.org/10.1016/j.engfailanal.2021.105554.
[3] Z. Han, L. Zhang, R. Azzam, J. Zhou, S. Wang, A statistical index indicating the degree and mechanical effects of grain size heterogeneity in rocks, Eng. Geol. 293 (2021) 106292, https://doi.org/10.1016/j.enggeo.2021.106292.
[4] Z. Gong, W. Zhao, K. Guan, P. Rao, Q. Zeng, J. Liu, Z. Feng, Influence of grain boundary and grain size on the mechanical properties of polycrystalline ceramics: Grain-scale simulations, J. Am. Ceram. Soc. 103 (10) (2020) 5900–5913, https://doi.org/10.1111/jace.17286.
[5] M. Groeber, S. Ghosh, M.D. Uchic, D.M. Dimiduk, A framework for automated analysis and simulation of 3D polycrystalline microstructures.: Part 1: Statistical characterization, Acta Mater. 56 (6) (2008) 1257–1273, https://doi.org/10.1016/j.actamat.2007.11.041.
[6] G. Rohrer, J. Li, S. Lee, A. Rollett, M. Groeber, M. Uchic, Deriving grain boundary character distributions and relative grain boundary energies from three-dimensional EBSD data, Mater. Sci. Technol. 26 (6) (2010) 661–669, https://doi.org/10.1179/026708309X12468927349370.
[7] M.I. Latypov, M. Kühbach, I.J. Beyerlein, J.-C. Stinville, L.S. Toth, T.M. Pollock, S.R. Kalidindi, Application of chord length distributions and principal component analysis for quantification and representation of diverse polycrystalline microstructures, Mater. Charact. 145 (2018) 671–685, https://doi.org/10.1016/j.matchar.2018.09.020.
[8] J. Segurado, R.A. Lebensohn, J. LLorca, Computational homogenization of polycrystals, Adv. Appl. Mech. 51 (2018) 1–114, https://doi.org/10.1016/bs.aams.2018.07.001.
[9] S. Bargmann, B. Klusemann, J. Markmann, J.E. Schnabel, K. Schneider, C. Soyarslan, J. Wilmers, Generation of 3D representative volume elements for heterogeneous materials: A review, Prog. Mater. Sci. 96 (2018) 322–384, https://doi.org/10.1146/annurev.matsci.37.052506.084401.
[10] T. Hatakeyama, K. Sawada, T. Hara, K. Sekido, K. Kimura, Three-dimensional analysis of the precipitation behavior of 18cr–9Ni–3Cu–Nb–N steel at 973 K, Scr. Mater. 200 (2021) 113904, https://doi.org/10.1016/j.scriptamat.2021.113904.
[11] A.J. Schwartz, M. Kumar, B.L. Adams, D.P. Field, Electron Backscatter Diffraction in Materials Science, vol. 2, Springer, 2009, https://doi.org/10.1007/978-0-387-88136-2.
[12] Y. Wang, J. Miller, Current developments and applications of micro-CT for the 3D analysis of multiphase mineral systems in geometallurgy, Earth-Sci. Rev. 211 (2020) 103406, https://doi.org/10.1016/j.earscirev.2020.103406.

[13] H.F. Poulsen, Multi scale hard x-ray microscopy, Curr. Opin. Solid State Mater. Sci. 24 (2) (2020) 100820, https://doi.org/10.1016/j.cossms.2020.100820.
[14] J. Kuhn, M. Schneider, P. Sonnweber-Ribic, T. Böhlke, Fast methods for computing centroidal laguerre tessellations for prescribed volume fractions with applications to microstructure generation of polycrystalline materials, Comput. Methods Appl. Mech. Engrg. 369 (2020) 113175, https://doi.org/10.1016/j.cma.2020.113175.
[15] K. Teferra, D.J. Rowenhorst, Optimizing the cellular automata finite element model for additive manufacturing to simulate large microstructures, Acta Mater. 213 (2021) 116930, https://doi.org/10.1016/j.actamat.2021.116930.
[16] F. Chen, H. Zhu, W. Chen, H. Ou, Z. Cui, Multiscale modeling of discontinuous dynamic recrystallization during hot working by coupling multilevel cellular automaton and finite element method, Int. J. Plast. 145 (2021) 103064, https://doi.org/10.1016/j.ijplas.2021.103064.
[17] T.M. Rodgers, D. Moser, F. Abdeljawad, O.D.U. Jackson, J.D. Carroll, B.H. Jared, D.S. Bolintineanu, J.A. Mitchell, J.D. Madison, Simulation of powder bed metal additive manufacturing microstructures with coupled finite difference-Monte Carlo method, Addit. Manuf. 41 (2021) 101953, https://doi.org/10.1016/j.addma.2021.101953.
[18] C. Marvel, C. Riedel, W. Frazier, A. Rollett, J. Rickman, M. Harmer, Relating the kinetics of grain-boundary complexion transitions and abnormal grain growth: A Monte Carlo time-temperature-transformation approach, Acta Mater. 239 (2022) 118262, https://doi.org/10.1016/j.actamat.2022.118262.
[19] S. Sunny, H. Yu, R. Mathews, A. Malik, W. Li, Improved grain structure prediction in metal additive manufacturing using a dynamic kinetic Monte Carlo framework, Addit. Manuf. 37 (2021) 101649, https://doi.org/10.1016/j.addma.2020.101649.
[20] S. Florez, K. Alvarado, B. Murgas, N. Bozzolo, D. Chatain, C.E. Krill III, M. Wang, G.S. Rohrer, M. Bernacki, Statistical behaviour of interfaces subjected to curvature flow and torque effects applied to microstructural evolutions, Acta Mater. 222 (2022) 117459, https://doi.org/10.1016/j.actamat.2021.117459.
[21] L.B. Mora, G. Gottstein, L. Shvindlerman, Three-dimensional grain growth: Analytical approaches and computer simulations, Acta Mater. 56 (20) (2008) 5915–5926, https://doi.org/10.1016/j.actamat.2008.08.006.
[22] R. Pei, S. Korte-Kerzel, T. Al-Samman, Normal and abnormal grain growth in magnesium: Experimental observations and simulations, J. Mater. Sci. Technol. 50 (2020) 257–270, https://doi.org/10.1016/j.jmst.2020.01.014.
[23] S. Florez, K. Alvarado, D.P. Muñoz, M. Bernacki, A novel highly efficient Lagrangian model for massively multidomain simulation applied to microstructural evolutions, Comput. Methods Appl. Mech. Engrg. 367 (2020) 113107, https://doi.org/10.1016/j.cma.2020.113107.
[24] N. Chandrappa, M. Bernacki, A level-set formulation to simulate diffusive solid/solid phase transformation in polycrystalline metallic materials-Application to austenite decomposition in steels, Comput. Mater. Sci. 216 (2023) 111840, https://doi.org/10.1016/j.commatsci.2022.111840.
[25] D. Tourret, H. Liu, J. LLorca, Phase-field modeling of microstructure evolution: Recent applications, perspectives and challenges, Prog. Mater. Sci. 123 (2022) 100810, https://doi.org/10.1016/j.pmatsci.2021.100810.
[26] R. Quey, P. Dawson, F. Barbe, Large-scale 3D random polycrystals for the finite element method: Generation, meshing and remeshing, Comput. Methods Appl. Mech. Engrg. 200 (17–20) (2011) 1729–1745, https://doi.org/10.1016/j.cma.2011.01.002.
[27] M. Groeber, S. Ghosh, M.D. Uchic, D.M. Dimiduk, A framework for automated analysis and simulation of 3D polycrystalline microstructures. Part 2: Synthetic structure generation, Acta Mater. 56 (6) (2008) 1274–12872, https://doi.org/10.1016/j.actamat.2007.11.040.
[28] A. Srivastava, H. Ghassemi-Armaki, H. Sung, P. Chen, S. Kumar, A.F. Bower, Micromechanics of plastic deformation and phase transformation in a three-phase TRIP-assisted advanced high strength steel: Experiments and modeling, J. Mech. Phys. Solids 78 (2015) 46–69, https://doi.org/10.1016/j.jmps.2015.01.014.
[29] A. Bagri, G. Weber, J.-C. Stinville, W. Lenthe, T. Pollock, C. Woodward, S. Ghosh, Microstructure and property-based statistically equivalent representative volume elements for polycrystalline Ni-based superalloys containing annealing twins, Metall. Mater. Trans. A 49 (11) (2018) 5727–5744, https://doi.org/10.1007/s11661-018-4858-y.
[30] M. Henrich, F. Pütz, S. Münstermann, A novel approach to discrete representative volume element automation and generation-DRAGen, Mater 13 (8) (2020) 1887, https://doi.org/10.3390/ma13081887.
[31] X. Tu, A. Shahba, J. Shen, S. Ghosh, Microstructure and property based statistically equivalent RVEs for polycrystalline-polyphase aluminum alloys, Int. J. Plast. 115 (2019) 268–292, https://doi.org/10.1016/j.ijplas.2018.12.002.
[32] M. Pinz, G. Weber, W. Lenthe, M. Uchic, T. Pollock, S. Ghosh, Microstructure and property based statistically equivalent RVEs for intragranular γ-γ'microstructures of Ni-based superalloys, Acta Mater. 157 (2018) 245–258, https://doi.org/10.1016/j.actamat.2018.07.034.
[33] K.A. Hart, J.J. Rimoli, Generation of statistically representative microstructures with direct grain geometry control, Comput. Methods Appl. Mech. Engrg. 370 (2020) 113242, https://doi.org/10.1016/j.cma.2020.113242.
[34] Y. Tang, Y. Xiong, S.-i. Park, D.W. Rosen, Universal material template for heterogeneous objects with applications to additive manufacturing, Comput. Aided Des. 129 (2020) 102929, https://doi.org/10.1016/j.cad.2020.102929.
[35] R.C. Foster, S. Vander Wiel, V. Anghel, C. Bronkhorst, Towards random generation of microstructures of spatially varying materials from orthogonal sections, Comput. Mater. Sci. 192 (2021) 110313, https://doi.org/10.1016/j.commatsci.2021.110313.
[36] D.T. Fullwood, S.R. Niezgoda, S.R. Kalidindi, Microstructure reconstructions from 2-point statistics using phase-recovery algorithms, Acta Mater. 56 (5) (2008) 942–948, https://doi.org/10.1016/j.actamat.2007.10.044.
[37] S.-Y. Chung, T.-S. Han, Reconstruction of random two-phase polycrystalline solids using low-order probability functions and evaluation of mechanical behavior, Comput. Mater. Sci. 49 (4) (2010) 705–719, https://doi.org/10.1016/j.commatsci.2010.06.014.
[38] Y. Jiao, N. Chawla, Modeling and characterizing anisotropic inclusion orientation in heterogeneous material via directional cluster functions and stochastic microstructure reconstruction, J. Appl. Phys. 115 (9) (2014) 093511, https://doi.org/10.1063/1.4867611.
[39] S. Chen, A. Kirubanandham, N. Chawla, Y. Jiao, Stochastic multi-scale reconstruction of 3D microstructure consisting of polycrystalline grains and second-phase particles from 2D micrographs, Metall. Mater. Trans. A 47 (3) (2016) 1440–1450, https://doi.org/10.1007/s11661-015-3283-8.
[40] V. Sundararaghavan, N. Zabaras, A dynamic material library for the representation of single-phase polyhedral microstructures, Acta Mater. 52 (14) (2004) 4111–4119, https://doi.org/10.1016/j.actamat.2004.05.024.
[41] V. Sundararaghavan, N. Zabaras, Classification and reconstruction of three-dimensional microstructures using support vector machines, Comput. Mater. Sci. 32 (2) (2005) 223–239, https://doi.org/10.1016/j.commatsci.2004.07.004.
[42] Z. Li, B. Wen, N. Zabaras, Computing mechanical response variability of polycrystalline microstructures through dimensionality reduction techniques, Comput. Mater. Sci. 49 (3) (2010) 568–581, https://doi.org/10.1016/j.commatsci.2010.05.051.
[43] B. Wen, N. Zabaras, A multiscale approach for model reduction of random microstructures, Comput. Mater. Sci. 63 (2012) 269–285, https://doi.org/10.1016/j.commatsci.2012.06.021.
[44] I. Javaheri, V. Sundararaghavan, Polycrystalline microstructure reconstruction using Markov random fields and histogram matching, Comput. Aided Des. 120 (2020) 102806, https://doi.org/10.1016/j.cad.2019.102806.
[45] I. Javaheri, M.T. Andani, V. Sundararaghavan, Large-scale synthesis of metal additively-manufactured microstructures using markov random fields, Comput. Mater. Sci. 206 (2022) 111228, https://doi.org/10.1016/j.commatsci.2022.111228.
[46] R. Bostanabad, Reconstruction of 3D microstructures from 2D images via transfer learning, Comput.-Aided Des. 128 (2020) 102906, https://doi.org/10.1016/j.cad.2020.102906.
[47] S. Patala, J.K. Mason, C.A. Schuh, Improved representations of misorientation information for grain boundary science and engineering, Prog. Mater. Sci. 57 (8) (2012) 1383–1425, https://doi.org/10.1016/j.pmatsci.2012.04.002.
[48] G. Nolze, R. Hielscher, Orientations–perfectly colored, J. Appl. Crystallogr. 49 (5) (2016) 1786–1802, https://doi.org/10.1107/s1600576716012942.

[49] A. Senthilnathan, V. Saseendran, P. Acar, N. Yamamoto, V. Sundararaghavan, Comparison and validation of stochastic microstructure characterization and reconstruction: Machine learning vs. deep learning methodologies, Acta Mater. 278 (2024) 120220, https://doi.org/10.1016/j.actamat.2024.120220.
[50] S. Patala, C.A. Schuh, A continuous and one-to-one coloring scheme for misorientations, Acta Mater. 59 (2) (2011) 554–562, https://doi.org/10.1016/j.actamat.2010.09.058.
[51] M. Groeber, S. Ghosh, M.D. Uchic, D.M. Dimiduk, A framework for automated analysis and simulation of 3D polycrystalline microstructures. Part 2: Synthetic structure generation, Acta Mater. 56 (6) (2008) 1274–1287, https://doi.org/10.1016/j.actamat.2007.11.041.
[52] A. Kumar, L. Nguyen, M. DeGraef, V. Sundararaghavan, A Markov random field approach for microstructure synthesis, Model. Simul. Mat. Sci. Eng. 24 (3) (2016) 035015, https://doi.org/10.1088/0965-0393/24/3/035015.
[53] P. Acar, V. Sundararaghavan, A Markov random field approach for modeling spatio-temporal evolution of microstructures, Model. Simul. Mat. Sci. Eng. 24 (7) (2016) 075005, https://doi.org/10.1088/0965-0393/24/7/075005.
[54] R. Bostanabad, Y. Zhang, X. Li, T. Kearney, L.C. Brinson, D.W. Apley, W.K. Liu, W. Chen, Computational microstructure characterization and reconstruction: Review of the state-of-the-art techniques, Prog. Mater. Sci. 95 (2018) 1–41, https://doi.org/10.1016/j.pmatsci.2018.01.005.
[55] P. Tahmasebi, A. Hezarkhani, M. Sahimi, Multiple-point geostatistical modeling based on the cross-correlation functions, Comput. Geosci. 16 (3) (2012) 779–797, https://doi.org/10.1007/s10596-012-9287-1.
[56] P. Tahmasebi, M. Sahimi, J. Caers, MS-CCSIM: accelerating pattern-based geostatistical simulation of categorical variables using a multi-scale search in Fourier space, Comput. Geosci. 67 (2014) 75–88, https://doi.org/10.1016/j.cageo.2014.03.009.
[57] A.A. Efros, W.T. Freeman, Image quilting for texture synthesis and transfer, in: Proceedings of the 28th Annual Conference on Computer Graphics and Interactive Techniques, 2001, pp. 341–346, https://doi.org/10.1145/383259.383296.
[58] K. Mahmud, G. Mariethoz, J. Caers, P. Tahmasebi, A. Baker, Simulation of earth textures by conditional image quilting, Water Resour. Res. 50 (4) (2014) 3088–3107, https://doi.org/10.1002/2013WR015069.
[59] M.J. Abdollahifard, B. Nasiri, Exploiting transformation-domain sparsity for fast query in multiple-point geostatistics, Comput. Geosci. 21 (2) (2017) 289–299, https://doi.org/10.1007/s10596-016-9612-1.
[60] J. Hoffimann, C. Scheidt, A. Barfod, J. Caers, Stochastic simulation by image quilting of process-based geological models, Comput. Geosci. 106 (2017) 18–32, https://doi.org/10.1016/j.cageo.2017.05.012.
[61] E. Baninajar, Y. Sharghi, G. Mariethoz, MPS-APO: a rapid and automatic parameter optimizer for multiple-point geostatistics, Stoch. Env. Res. Risk Assess. 33 (11) (2019) 1969–1989, https://doi.org/10.1007/s00477-019-01742-7.
[62] G.-J. Yuan, H. Chen, D.-F. Li, C.-Y. Gong, X.-C. Zhang, S.-T. Tu, The effect of δ phase on the microplasticity evolution of a heat-treated nickel base superalloy, Mech. Mater. 148 (2020) 103520, https://doi.org/10.1016/j.mechmat.2020.103520.
[63] G.-J. Yuan, R.-Z. Wang, W.-B. Zhu, D.-F. Li, Y. Zhang, X.-C. Zhang, S.-T. Tu, Experimental and simulated investigations of low cycle fatigue behavior in a nickel-based superalloy with different volume fractions of δ phase, Int. J. Fatigue 153 (2021) 106411, https://doi.org/10.1016/j.ijfatigue.2021.106411.
[64] R.-H. Song, H.-L. Qin, D.-F. Li, Z.-N. Bi, E.P. Busso, H.-Y. Yu, X.-L. Liu, J.-h. Du, J. Zhang, An experimental and numerical study of quenching-induced residual stresses under the effect of dynamic strain aging in an IN718 superalloy disc, J. Eng. Mater. Technol. 144 (1) (2022) 011002, https://doi.org/10.1115/1.4051086.
[65] R.-H. Song, H.-L. Qin, Z.-N. Bi, J. Zhang, H. Chi, E.P. Busso, D.-F. Li, Experimental and numerical investigations of dynamic strain ageing behaviour in solid solution treated inconel 718 superalloy, Eng. Comput. 38 (1) (2021) 19–35, https://doi.org/10.1108/EC-01-2020-0006.
[66] D.-F. Li, N.P. O'Dowd, On the evolution of lattice deformation in austenitic stainless steels—The role of work hardening at finite strains, J. Mech. Phys. Solids 59 (12) (2011) 2421–2441, https://doi.org/10.1016/j.jmps.2011.09.008.
[67] D.-F. Li, C.M. Davies, S.-Y. Zhang, C. Dickinson, N.P. O'Dowd, The effect of prior deformation on subsequent microplasticity and damage evolution in an austenitic stainless steel at elevated temperature, Acta Mater. 61 (10) (2013) 3575–3584, https://doi.org/10.1016/j.actamat.2013.02.038.
[68] H.-J. Guo, C. Ling, E.P. Busso, Z. Zhong, D.-F. Li, Crystal plasticity based investigation of micro-void evolution under multi-axial loading conditions, Int. J. Plast. 129 (2020) 102673, https://doi.org/10.1016/j.ijplas.2020.102673.
[69] H.-J. Guo, C. Ling, D.-F. Li, C.-F. Li, Y. Sun, E.P. Busso, A data-driven approach to predicting the anisotropic mechanical behaviour of voided single crystals, J. Mech. Phys. Solids 159 (2022) 104700, https://doi.org/10.1016/j.jmps.2021.104700.
[70] Y. Zhang, H. Chen, Y.-F. Jia, D.-F. Li, G.-J. Yuan, X.-C. Zhang, S.-T. Tu, A modified kinematic hardening model considering hetero-deformation induced hardening for bimodal structure based on crystal plasticity, Int. J. Mech. Sci. 191 (2021) 106068, https://doi.org/10.1016/j.ijmecsci.2020.106068.
[71] G. Martin, N. Ochoa, K. Sai, E. Hervé-Luanco, G. Cailletaud, A multiscale model for the elastoviscoplastic behavior of directionally solidified alloys: Application to FE structural computations, Int. J. Solids Struct. 51 (5) (2014) 1175–1187, https://doi.org/10.1016/j.ijsolstr.2013.12.013.
[72] A. Ullah, G. Liu, J. Luan, W. Li, M. ur Rahman, M. Ali, Three-dimensional visualization and quantitative characterization of grains in polycrystalline iron, Mater. Charact. 91 (2014) 65–75, https://doi.org/10.1016/j.matchar.2014.02.009.
[73] D.T. Fullwood, S.R. Niezgoda, B.L. Adams, S.R. Kalidindi, Microstructure sensitive design for performance optimization, Prog. Mater. Sci. 55 (6) (2010) 477–562, https://doi.org/10.1016/j.pmatsci.2009.08.002.